DATA-DRIVEN POPULATION INFERENCE FROM GRAVITATIONAL-WAVE SOURCES & ELECTROMAGNETIC COUNTERPARTS

by

Siddharth Mohite

A Dissertation Submitted in

Partial Fulfillment of the

Requirements for the Degree of

Doctor of Philosophy

in Physics

at

The University of Wisconsin-Milwaukee

August 2022

ABSTRACT

DATA-DRIVEN POPULATION INFERENCE FROM GRAVITATIONAL-WAVE SOURCES & ELECTROMAGNETIC COUNTERPARTS

by

Siddharth Mohite

The University of Wisconsin-Milwaukee, 2022
Under the Supervision of Professor Jolien Creighton, PhD

Gravitational-wave (GW) astronomy has presented an unprecedented way to view the universe and study populations of astrophysical objects such as merging compact binaries containing black holes (BHs) and neutron stars (NSs). With the latest catalog of observations detected by the Advanced LIGO-Virgo detector network, recent analyses are placing interesting constraints on the population of BHs and NSs in these binaries. In particular, we are learning a great deal about how these binaries are distributed as a function of their masses. Another aspect of GW astronomy that has the potential to provide insights into fundamental physics is the multi-messenger follow up of the potential "kilonova" from binary mergers involving NSs. Observations or non-detections of kilonovae can be used to learn more about the formation of heavy elements via r-process nucleosynthesis as well as to shed light on the inner mechanisms of such mergers. This dissertation presents two studies that focus on inferring population properties from compact binaries using data-driven methods. The first is using the flexible approach of Gaussian processes to model the mass distribution of compact binaries and the second is developing a hierarchical Bayesian inference framework to infer kilonova population properties using non-detections in electromagnetic surveys.

TABLE OF CONTENTS

LIST OF FIGURES

LIST OF TABLES

LIST OF ABBREVIATIONS

GW	Gravitational-wave
EM	Electromagnetic
GWs	Gravitational-waves
CBC	Compact Binary Coalescence
BBH	Binary Black Hole
BNS	Binary Neutron Star
NSBH	Neutron Star - Black Hole
GP	Gaussian Process
BGP	Binned Gaussian Process
KN	Kilonova
KNe	Kilonovae
SNR	Signal-to-Noise Ratio

ACKNOWLEDGMENTS

I would like to thank my advisors at UWM — Jolien Creighton and David Kaplan — for their constant guidance, support and encouragement. Thanks for always keeping your door open to answer any questions and thank you for being patient with me while I figured things out. Thank you for giving me the opportunity to be a part of the LIGO and GROWTH Collaborations and for the freedom to work on projects that became a part of this dissertation.

Graduate life is incomplete without friends who share the journey and add fun to coursework and research. I would like to thank Shasvath Kapadia, Deep Chatterjee, Adil Amin, Casey McGrath, Alex McEwen, Ian Brown, Caitlin Rose, Brandon Piotrzkowski, Danika Holmes for their friendship, collaboration and support through my time here at UWM.

The successful completion of my PhD journey would not have been possible without the people, resources and environment at the Department of Physics and CGCA at UWM. Special thanks to Heidi Matera and Kate Valerius for always being there for any form of support and for being constant well-wishers.

I am indebted to two programs that have given me some of my best academic experiences and skills that will stand me in good stead for the future. The LSST Data Science Fellowship Program has broadened my horizons within astronomy and astrophysics by making me a part of a vibrant community filled with amazing people working on diverse projects. It has also enabled me with skills in preparation for the era of big data in astronomy and which have contributed in me achieving success in my research projects. The Center for Computational Astrophysics (CCA) Pre-Doctoral Fellowship Program intro-

duced me to one of my best research mentors so far in life — Chiara Mingarelli — who has supported me throughout the last two years and gone out of her way to find opportunities for me. I have benefited the most from her constant encouragement and excitement in our work.

I would like to acknowledge support from the NSF grant NSF PHY #1912649. I am also grateful for computational resources provided by the Leonard E Parker Center for Gravitation, Cosmology and Astrophysics at the University of Wisconsin-Milwaukee. Acknowledgements also to the NSF Cybertraining Grant #1829740, the Brinson Foundation, and the Moore Foundation.

Lastly, but most importantly, the deepest gratitude is towards my partner, best friends and family. I would never have made it here if it was not for all of you.

CHAPTER 1

Introduction

Gravitational-waves (GWs), which are perturbations in the space-time metric are a direct consequence of Einstein's general theory of relativity (Einstein, 1916). The theory predicted that these perturbations travel at the speed of light. However, it took several decades of theoretical and observational advancements to be able to appreciate the gravitational radiation emitted by compact binaries which are the focus of this dissertation. The binary pulsar system PSR 1913+16 observed in 1975 (Hulse & Taylor, 1975) provided the first opportunity to test the predictions of GWs and general relativity in the strong-field regime. Since then observations of this system have shown that the period of the binary orbit is decreasing at a rate that is in excellent agreement with that predicted by the loss of energy through GWs for the system (Weisberg & Taylor, 2005).

The development and construction of ground-based observatories to detect GWs began in the 1990s with the setup of the Initial Laser Interferometer Gravitational-wave Observatory (LIGO) (Abramovici et al., 1992). In parallel, a global network of GW detectors was also established with the construction of the Virgo observatory near Pisa, Italy (Acernese et al., 2006) ; the TAMA300 interferometer near Tokyo, Japan (Takahashi & TAMA Collaboration, 2004) and the GEO600 interferometer near Hannover, Germany (Lück et al., 2006). With subsequent commissioning in the early 2000s, Initial LIGO and Virgo conducted joint science observing runs (in particular from November 2005 to September 2007) called S5 and VSR1 respectively, to search for potential sources of GWs and set upper limits (The LIGO Scientific Collaboration & The Virgo Collaboration, 2009; Abadie et al., 2010b; The LIGO Scientific Collaboration et al., 2010; Abadie et al., 2010a).

The sources of GWs that can be detected by such GW observatories include inspi-

ralling compact binaries like PSR 1913 + 16 that contain either neutron stars (NSs) or black holes (BHs) as its components, rotating non-axisymmetric neutron stars, primordial GW radiation from the early universe and core-collapse supernovae (Cutler & Thorne, 2002). In general, there are three types of compact binaries that are potential sources of GWs : a binary neutron star (BNS), binary black hole (BBH) or a neutron star - black hole binary (NSBH).

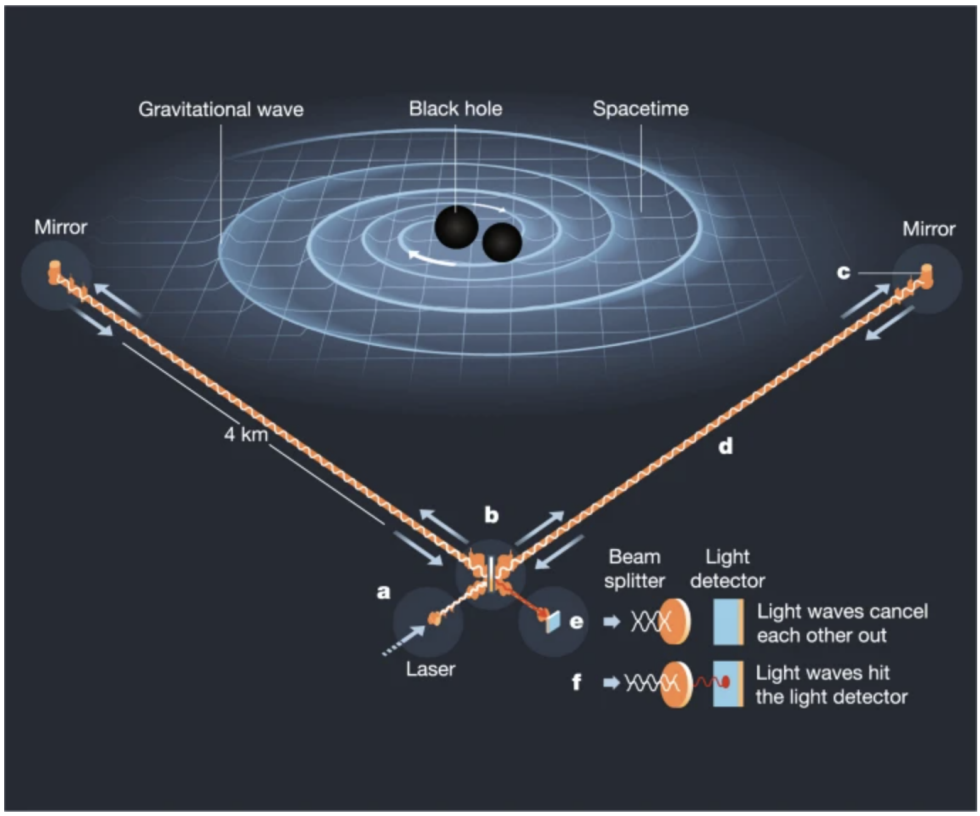

Figure 1.1: Setup of Gravitational-wave observatories from Miller & Yunes (2019). Image Credit:Johan Jarnestad/The Royal Swedish Academy of Sciences

At its heart, gravitational-wave observatories are essentially Michelson interferometers. Figure 1.1 shows the general setup of these interferometers and how GW radiation from compact binaries are detected. The interferometers have an L-shaped configuration

of orthogonal arms with length (L) across which laser light is sent. Each arm has a suspended mirror at the end and serves as a test mass. When gravitational waves emitted by sources such as compact binaries arrive at the detectors, they produce a differential change in the length of one arm relative to the other (ΔL). Thus, a corresponding strain ($\frac{\Delta L}{L}$) can be measured. In practice, the resulting interference pattern is used to decipher the amplitude of the gravitational-wave strain as well as its phase. LIGO consists of two such interferometer setups across the United states with 4 kilometer long arms - one in Hanford, Washington and the other in Livingston, Louisiana. The Virgo interferometer has ~ 3 kilometer arms while TAMA300 and GEO600 have 300 meter and 600 meter arms respectively. Some of these interferometers are shown in Figure 1.2.

Figure 1.2: Views of the gravitational-wave observatories LIGO (left, center) and Virgo (right)

1.1 THE ADVANCED DETECTOR ERA : DAWN OF GRAVITATIONAL-WAVE ASTRONOMY

The Initial LIGO and Virgo searches attained a GW strain sensitivity of $\sim 10^{-21}$ along with a distance range of ~ 30 Mpc (Initial LIGO) and ~ 8 Mpc (Virgo) for an optimally oriented

BNS system having component masses of $1.4M_{\odot}$ each. Significant upgrades in sensitivity resulted in the replacement of Initial LIGO and Virgo to their advanced counterparts - Advanced LIGO (aLIGO) in 2015 and Advanced Virgo (aVirgo) in 2017. For aLIGO, these upgrades resulted in strain sensitivity improvements by a factor of ~ 10 and made the detectors capable of detecting a typical BNS system within ~ 190 Mpc. Also, the sensitivity improvement resulted in the extension of the sensitive band at the low-frequency end from 40 Hz to 10 Hz. The stage was thus set to detect GWs for the first time.

Gravitational-wave (GW) astronomy was established in a watershed moment in September 2015 with the first observation of a BBH merger by the aLIGO detector network (Abbott et al., 2016c). This unprecedented event, detected almost a century after Einstein's theoretical work describing GWs, extended the frontier of observational astronomy and vindicated decades of efforts by researchers working on GW science. Over the course of the last 7 years, the total count of compact binary mergers detected in the Advanced detector era stands at ~ 90 (The LIGO Scientific Collaboration et al., 2021a). aLIGO began with its first observing run (O1) from September 2015 to January 2016 (Abbott et al., 2016b) which yielded 3 BBH detections. The second observing run (O2) from November 2016 to August 2017 (Abbott et al., 2019a) witnessed the observation of 7 BBH mergers. aVirgo joined the observation efforts in August 2017. In what was another milestone event in GW astronomy, O2 saw the first detection of a BNS merger (GW170817) on 17 August 2017 (Abbott et al., 2017b). This event is particularly important as it marked the beginning of multi-messenger astronomy in the context of GW events which is another focus of this dissertation. The third observing run (O3) of aLIGO and aVirgo from April 2019 to March 2020 resulted in the detection of an additional ~ 80 compact binary mergers. These include several interesting events such as another BNS (GW190425; Abbott et al. 2020a), the first confirmed detections of an NSBH system (GW200105 and GW200115; Abbott et al.

2021f) and the first unambiguously detected asymmetric mass merger (GW190412; Abbott et al. 2020d). The discovery of such a large number of sources naturally leads to the question — what can we infer about the population of these sources from their individual observations? This dissertation focuses on one such aspect of the population of compact binaries, namely the astrophysical distribution of these GW sources as a function of their masses.

1.2 COMPACT-OBJECT BINARIES AS SOURCES OF GRAVITATIONAL WAVES

The coalescence of binary systems consisting of compact objects such as black holes or neutron stars are the most promising sources of GWs that can be detected by ground-based observatories. One aspect that makes these sources promising is the fact that the strain waveform expected from such systems is known very well from theory and numerical relativity.

Here we reproduce some of the derivation from Chapter 3 of Creighton & Anderson (2011) to highlight the dependence of the waveform from a fiducial compact binary system in terms of the binary parameters. The waveform can be divided into 3 phases — inspiral, merger and ringdown. The inspiral phase is when the motion of the binary components is not too relativistic. Such a phase can be modeled using Post-Newtonian (PN) theory. As the binary transitions from the inspiral to the merger phase, the component velocities become highly-relativistic and are comparable to the speed of light. PN methods ultimately fail to capture the evolution in this phase and we must rely on numerical relativity to solve for the waveform. Furthermore for systems containing neutron stars tidal interactions with the binary companion become important. Also, precession and spin-orbit couplings can give rise to complex waveforms that need to be accounted for in the analytic PN approximation of the waveforms. Finally, the merger of the two compo-

nents in the binary results in the formation of a black hole which releases GW radiation before settling to a stationary state. The GW radiation and waveform in this ringdown phase can be obtained analytically using the quasi-normal modes of the final black hole. Figure 1.3 shows these phases and the expected GW strain amplitude waveform for the first ever BBH event to be detected - GW150914 (Abbott et al., 2016c).

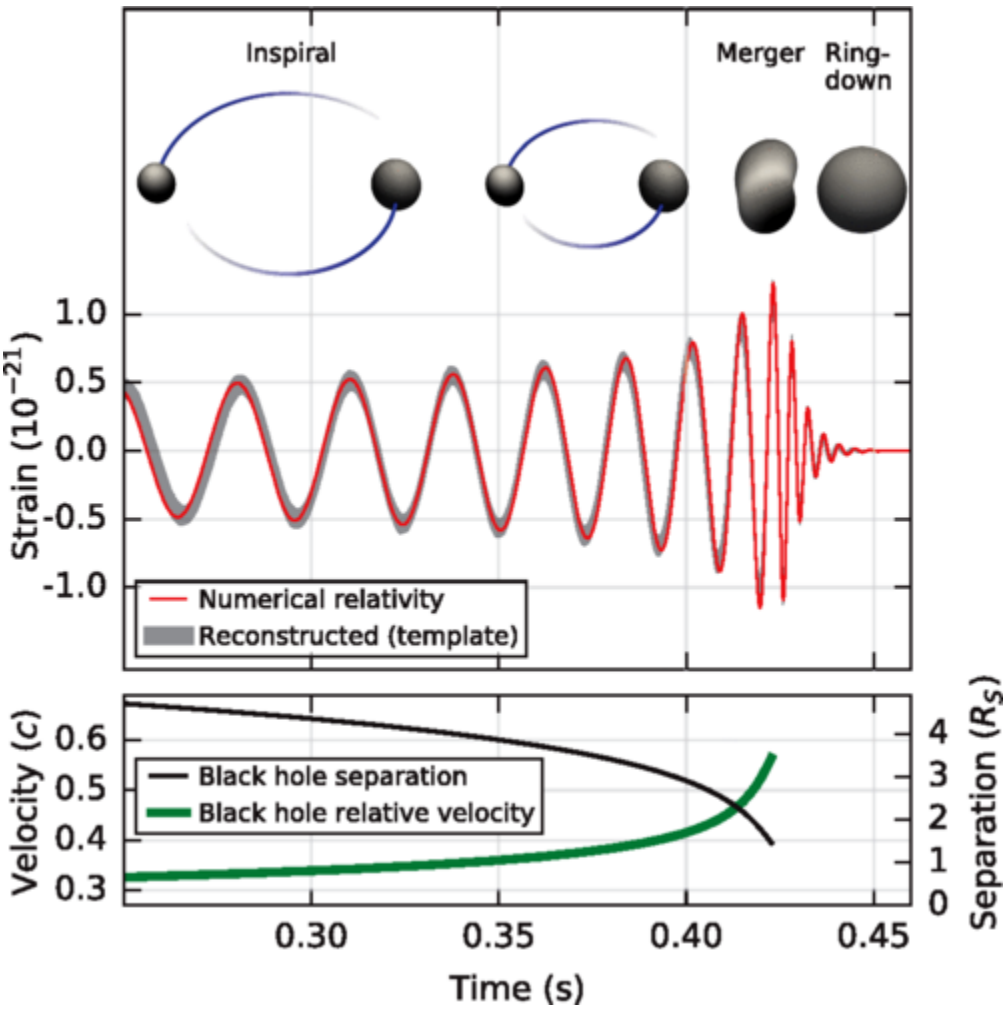

Figure 1.3: Reproduced from Abbott et al. (2016c). Top: Estimated GW strain amplitude for GW150914 and a representation of the three phases in binary evolution. Bottom : Relative separation and velocity between the BH components computed using numerical relativity.

In the far-field zone where the distance (r) between the source and observer is much

larger than the GW wavelength as well as the source size/separation, the metric perturbation under the linear approximation becomes,

$$h_{ij}^{TT}(t) = \frac{2G}{c^4 r}\ddot{I}_{ij}^{TT}(t - r/c) \tag{1.1}$$

where G is the gravitational constant, c is the speed of light, r is the distance to the source and I_{ij} is the quadrupole moment tensor of the mass distribution ρ producing the GWs given by,

$$I^{ij}(t) = \int x^i x^j \rho(t - r/c, x) d^3x. \tag{1.2}$$

Eqn. 1.1 highlights the important fact that the metric perturbations for GWs depend on the time varying quadrpole moment of the source. Moreover, the quadrapole is the lowest multipole that contributes towards GW emission which is in contrast to electromagnetic (EM) emission where changing dipoles can exist. The superscript 'TT' in the equations above denote the Transverse-Traceless gauge. In this gauge the metric perturbation is transverse to the direction of propagation and is traceless. We assume that quantities that follow are evaluated in this gauge. We also define the traceless reduced quadrapole moment tensor $\mathcal{I}^{ij}$ as,

$$\mathcal{I}^{ij}(t) = \int \left(x^i x^j - \frac{1}{3} r^2 \delta^{ij}\right) \rho(t - r/c, x) d^3x. \tag{1.3}$$

The gravitational-wave flux which is the gravitational energy $dE_{\rm GW}$ passing through an area dA in time dt is then given as,

$$\frac{dE_{\rm GW}}{dAdt} = -\frac{c^3}{32\pi G}\langle \dot{h}_{TT}^{ij} \dot{h}_{ij}^{TT} \rangle \tag{1.4}$$

$$= -\frac{G}{8\pi c^5 r^2}\langle \dddot{I}^{ij}_{TT}\, \dddot{I}^{TT}_{ij}\rangle. \tag{1.5}$$

This gives the gravitational-wave luminosity as,

$$L_{\rm GW} = -\frac{dE_{\rm GW}}{dt} = \frac{G}{5c^5}\langle \dddot{I}_{ij}\, \dddot{I}^{ij}\rangle. \tag{1.6}$$

Here $\langle ...\rangle$ denotes an average over a spacetime region containing several GW oscillations or wavelengths. Now, let us assume that a binary system consists of two point particles with masses m_1 and m_2. Let a, ϕ, M, μ, i be the orbital separation, orbital phase, total mass ($M = m_1 + m_2$), reduced mass ($\mu = \frac{m_1 m_2}{M}$) and inclination with respect to the observer of the binary, respectively. Then for a circular binary orbit and observer at distance r, the metric perturbations in the two GW polarizations are given as,

$$h_+ = -\tfrac{2G\mu}{c^2 r}\,(1+\cos^2 i)\left(\tfrac{v}{c}\right)^2 \cos(2\phi), \tag{1.7}$$

$$h_\times = -\tfrac{4G\mu}{c^2 r}\cos i\left(\tfrac{v}{c}\right)^2 \sin(2\phi) \tag{1.8}$$

where v is the orbital velocity of the components. A point to note is that GW emission is monochromatic with a frequency that is twice the orbital frequency since $f_{\rm GW} = 2f_{\rm orb} = \frac{\omega}{\pi}$; where $\phi = \omega t$. The luminosity $L_{\rm GW}$ of the binary at any given time is given as,

$$L_{\rm GW} = \frac{32}{5}\frac{c^5}{G}\eta^2\left(\frac{v}{c}\right)^{10} \tag{1.9}$$

where $\eta = \frac{\mu}{M}$ is the symmetric mass ratio of the binary. Using $E_{GW} = -\frac{1}{2}\mu v^2$ and Eqn. 1.6 we get,

$$\frac{d(v/c)}{dt} = \frac{32}{5}\frac{c^3}{GM}\eta\left(\frac{v}{c}\right)^9. \tag{1.10}$$

We can then evaluate the time to coalescence (t_c) of the binary from a fiducial initial velocity v_o by integrating Eqn. 1.10 as,

$$\int_{v_o/c}^{\infty} \frac{d(v/c)}{(v/c)^9} = \frac{32}{5}\frac{c^3}{GM}\eta \int_0^{t_c} dt. \tag{1.11}$$

Solving the above equation and noting that $f_{\rm GW} = \frac{v^3}{\pi GM}$ gives us the time to coalescence in terms of orbital velocity and frequency,

$$t_c = \frac{5}{256\eta}\frac{GM}{c^3}\left(\frac{v_o}{c}\right)^{-8} \tag{1.12}$$

$$= \frac{5}{256\eta}\frac{GM}{c^3}\left(\frac{\pi GM f_o}{c^3}\right)^{-8/3}. \tag{1.13}$$

Although the orbit of the binary decays, the frequency and amplitude of the GW emission will increase. This can be seen for the case of the waveform called the Newtonian chirp which is the leading order expansion of the equations above. For the chirp waveform, the GW frequency evolution can be obtained by noting that $f_{\rm GW} = \frac{v^3}{\pi GM}$. This gives,

$$\frac{df_{\rm GW}}{dt} = \frac{df_{\rm GW}}{dv}\frac{dv}{dt} \tag{1.14}$$

$$= \left(\frac{3v^2}{\pi GM}\right)\left(\frac{32\eta}{5}\frac{c^4}{GM}\left(\frac{v}{c}\right)^9\right) \tag{1.15}$$

$$= \frac{96}{5}\pi^{8/3}\eta\left(\frac{GM}{c^3}\right)^{5/3} f_{\rm GW}^{11/3}. \tag{1.16}$$

The combination $\eta^{3/5}M$ represents a mass representation called the chirp mass $\mathcal{M}_c$. We thus get,

$$\frac{df_{\rm GW}}{dt} = \frac{96}{5}\pi^{8/3}\left(\frac{G\mathcal{M}_c}{c^3}\right)^{5/3} f_{\rm GW}^{11/3}. \tag{1.17}$$

At Newtonian order, the chirp mass is the only mass combination that defines the frequency evolution and chirp waveform. Since the phase evolution is directly related to the frequency, the chirp mass is the only parameter that can be measured from the amplitude and phase at this order. For higher post-Newtonian orders, other mass combinations become important as well. We conclude the derivation by giving the full form of the GW polarizations at Newtonian order :

$$h_+ = -\frac{G\mathcal{M}_c}{c^2 r}\frac{1+\cos^2 i}{2}\left(\frac{c^3(t_c-t)}{5G\mathcal{M}_c}\right)^{-1/4}\cos\left[2\phi_c - 2\left(\frac{c^3(t_c-t)}{5G\mathcal{M}_c}\right)^{5/8}\right], \tag{1.18}$$

$$h_\times = -\frac{G\mathcal{M}_c}{c^2 r}\cos i\left(\frac{c^3(t_c-t)}{5G\mathcal{M}_c}\right)^{-1/4}\sin\left[2\phi_c - 2\left(\frac{c^3(t_c-t)}{5G\mathcal{M}_c}\right)^{5/8}\right]. \tag{1.19}$$

1.3 GW170817 AND AT2017GFO : BIRTH OF MULTI-MESSENGER ASTRONOMY

Compact binary systems containing neutron stars are of particular importance since they not only have the potential to be detected in the GW spectrum but also have been theorized to emit in the EM spectrum in the aftermath of the merger (Li & Paczyński, 1998; Rosswog, 2005; Metzger et al., 2010; Tanaka & Hotokezaka, 2013). Such mergers have the capability to inform important topics in nuclear theory such as the formation of heavy elements in the periodic table via r-process nucleosynthesis (Côté et al., 2018; Hotokezaka et al., 2018; Radice et al., 2018; Tanaka et al., 2018) and the nuclear equation of state (Foucart et al., 2018; Coughlin et al., 2018b; Radice & Dai, 2019; Hinderer et al., 2019). Also, since the luminosity distance of a GW source is a direct observable from the GW strain amplitude, following up NS mergers in the EM spectrum can have implications for cos-

mology. This is because EM observations can help provide a redshift for the merger event and combined with an estimate of the luminosity distance can deliver an independed measurement of the Hubble constant. In Section 1.1, we mentioned the detection of the first BNS system — GW170817 (Abbott et al., 2017b). This event also signalled the dawn of multi-messenger GW astronomy as it was the first event to be jointly detected in both spectra with its EM counterparts being detected over a wide range of wavelengths (Abbott et al., 2017c). This dissertation focuses on one such EM counterpart called the kilonova (Metzger et al., 2010).

1.4 DISSERTATION OUTLINE

With current gravitational-wave observatories already generating catalogs of sources, we are in an era where we can leverage these rich datasets of events to place important astrophysical constraints. On the other hand, the search for mergers containing neutron stars in both the GW and EM spectra holds the promise of advancing the frontiers of multi-messenger astronomy. Developing frameworks of inference to be "data-driven" instead of being "model-driven" has the advantage of learning new features about the population of these events without having to tune our models. This dissertation presents novel methods to analyze two different populations that arise from GW and EM counterpart observations.

The disseration is organized as follows : Chapter 2 presents a method to model the two-dimensional (2-D) mass distribution of compact binaries observed by aLIGO and aVirgo using Gaussian Processes (GPs). It contains a description of the GP basics, application of GPs to GW catalogs of events and selection biases in GW population inference. The method was applied to the latest catalog of GW observations (The LIGO Scientific Collaboration et al., 2021a) and corresponding results which appeared in a collaboration

manuscript (Abbott et al., 2021a) are presented. Chapter 3 presents a novel framework based on hierarchical Bayesian inference that places constraints on kilonova population properties. It describes how EM non-detections of binary mergers containing NSs can be leveraged. Chapter 4 concludes by outlining the limitations of the current implementation of these methods that can be improved keeping future catalogs in mind.

Publications Connected to this Dissertation

The work presented in **Chapters 2 and 3** was published in the following:

Abbott R., et al., (2021). *The population of merging compact binaries inferred using gravitational waves through GWTC-3*.

→ http://dx.doi.org/10.48550/ARXIV.2111.03634

→ https://arxiv.org/abs/2111.03634

→ I contributed all of the results for the BINNED GAUSSIAN PROCESS model appearing in this manuscript. These have been reproduced in Section 2.4 of Chapter 2. I contributed to writing parts of Sections III.C.4, IV, Appendix A and the entirety of Appendix B.1.e. I prepared Figure 4 of the manuscript.

Mohite S. R., et al., (2022). *Inferring kilonova population properties with a hierarchical Bayesian framework I : Non-detection methodology and single-event analyses*.

→ http://dx.doi.org/10.3847/1538-4357/ac3981

→ https://arxiv.org/abs/2107.07129

→ My contributions to this publication include writing $\sim 80\%$ of the text, preparing Figures 1,2,4, the right panel of Figure 5 and preparing Table 1. In addition, I was responsible for all of the calculations, results and code related to the `nimbus` formalism presented in the publication. I was the corresponding author. This publication is reproduced in part in Chapter 3.

CHAPTER 2

Gaussian Processes : A Tool to Infer Binary Compact-object Mass Distributions

The results presented in Section 2.4 in this chapter have been reproduced using the public data release (LIGO Scientific Collaboration et al., 2021) for the collaboration manuscript Abbott et al. (2021a).

2.1 INTRODUCTION

Recent analyses of GW observations (Abbott et al., 2019d, 2021e) have already started placing interesting constraints on the population of compact binaries detectable by Advanced LIGO-Virgo and their associated merger rates. These studies have relied on two key features (i) employing parametric models for the binary black hole (BBH) distribution that rely on specific parameters to determine the shape of the distribution (Kovetz et al., 2017; Fishbach & Holz, 2017; Talbot & Thrane, 2018), and (ii) analyzing populations of the three types of compact binary systems; BBHs, BNSs and NSBHs, independently (Abbott et al., 2019a, 2021e).

However, parametric models have the caveat that they cannot incorporate deviations from a specific functional form in the case where a new event added in the analysis drastically changes the nature of the distribution. Furthermore, with the increasing number of GW events being detected, the possibility of correlations between sub-populations such as NSBHs and BBHs highlights the need to model all compact binaries within the same formalism in order to infer the presence of features such as mass gaps in the spectrum (Özel & Freire, 2016; Freire et al., 2008; Margalit & Metzger, 2017; Heger & Woosley, 2002;

Heger et al., 2003; Fishbach & Holz, 2017; Talbot & Thrane, 2018; Wysocki et al., 2019). Previous studies in the literature (Mandel et al., 2016; Wysocki et al., 2019; Tiwari, 2021) have outlined methods to model the spectrum of compact binaries using flexible methods such as Gaussian mixture models and Gaussian processes (Rasmussen & Williams, 2005) that do not rely on a definite shape of the function being modeled. Such methods, as we will see in this chapter, allow us to simultaneously fit for the merger rates as well as the population distribution. Building on these previous efforts, the work presented in this chapter will focus on describing such a flexible framework based on Gaussian processes to model the mass distribution of these binaries across all multiple populations.

This chapter is organized as follows : In Section 2.2 we give an introduction to the concept of Gaussian Processes (GPs) and how they can be used to model unknown functions. Section 2.3 describes the BINNED GAUSSIAN PROCESS model and its underlying parameters. The specific prior choices used in the inference are also described here. We also use this section to derive the form of the posterior distribution for the associated hyper-parameters of the BGP model. The important aspect of selection effects in GW population inference and how they are incorporated in our analysis is also outlined. Section 2.4 shows the results obtained by using the BGP model to infer the population of compact binaries using data from Advanced LIGO-Virgo's latest gravitational wave catalog (The LIGO Scientific Collaboration et al., 2021a). In particular, we present results for merger rate densities across various mass ranges and sub-populations as well as the mass distribution of compact binaries. We conclude in Section 2.5 with a discussion and note on how the BGP model can be improved keeping future GW catalogs in mind.

2.2 GAUSSIAN PROCESS BASICS

For a mathematical definition, suppose we consider obtaining data($\vec{y}$) at a set of observation points X. In general, the points in X could be multi-dimensional (as we will see in Section 2.3.1). Then a Gaussian process (GP) model for this data assumes that the data($\vec{y}$) are distributed as a multi-variate Gaussian distribution with a mean value $\mu(X)$ at each observation point and a covariance matrix Σ. As is standard of Gaussian distributions, $\mu(X)$ sets the mean amplitude at points in parameter space while the covariance matrix Σ determines the two-point correlation between pairs of points in X. Thus, it is useful to denote the covariance matrix as $\Sigma(X, X)$. The covariance matrix influences the level of smoothness and thereby the space of functions spanned by the GP.

The covariance matrix requires a kernel function $k(x, x')$ that can generate values for the covariance value between any two points x and x' in the set X. Writing this explicitly gives,

$$\Sigma = \begin{bmatrix} k(x_0, x_0) & k(x_0, x_1) & \dots \\ \vdots & \ddots & \\ k(x_{N-1}, x_0) & \dots & k(x_{N-1}, x_{N-1}) \end{bmatrix}. \tag{2.1}$$

One of the most commonly used kernel functions is the Radial Basis Function (RBF), Squared Exponential or Quadratic Exponential Kernel which is of the form:

$$k(x, x') = \sigma^2 \exp\left(\frac{-(x - x')^2}{2l^2}\right). \tag{2.2}$$

We can see that there are 2 parameters that define the kernel function in this case — σ which controls the overall amplitude of covariance and l which controls the width. It is this parameter l that has a direct influence on the shape of functions drawn from the

GP whose covariance is determined by such a kernel function (see Figure 2.2). Eqn. 2.3 shows the definition of a GP where the data $\vec{y}$ are distributed as a multi-variate Gaussian distribution. Here $\mathcal{N}$ is used to denote the Gaussian distribution,

$$\vec{y} \sim \mathcal{N}(\mu(X), \Sigma(X, X)). \tag{2.3}$$

Extending the notion of the set X to contain an infinite number of points in the relevant parameter space, we can see that Eqns. 2.1, 2.2 and 2.3 enable the multi-variate Gaussian distribution to be evaluated across the entire parameter space of interest. Defined in this way, every random draw from such a GP is a unique function as shown in Figure 2.1. GPs thus return a distribution over functions with the measured values of $\vec{y}$ informing inferences on the two quantities that define the GP — μ and Σ.

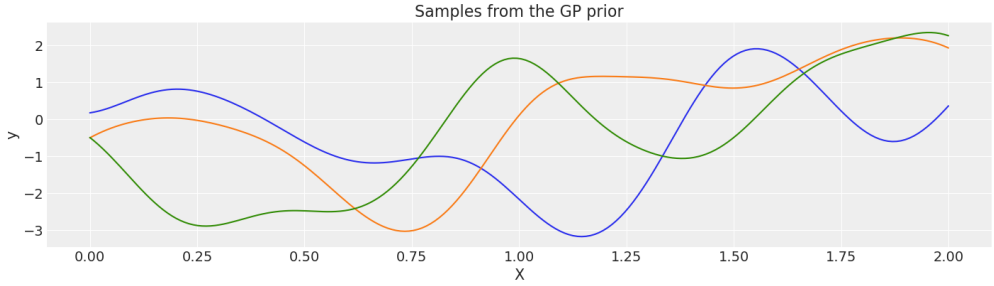

Figure 2.1: Three random draws from a Gaussian Process resulting in 3 unique functions. The mean function μ is fixed to be 0 at all points while a RBF kernel (Eqn. 2.2) is used for the covariance with $\sigma = 2$ and $l = 0.2$. Reproduced using code from https://www.pymc.io/.

As shown in Figure 2.2, smaller values of l tend to favor functions that vary more over a given region of parameter space while larger values of l favor functions that do not evolve as fast. Thus, GPs offer a flexible way to model functions with unknown amplitudes and shapes.

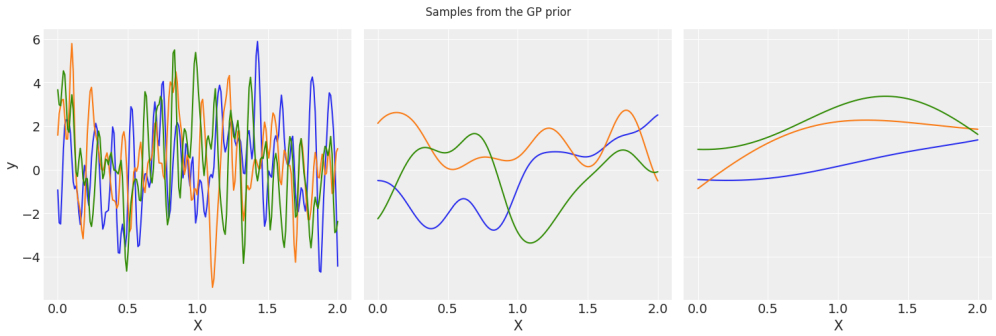

Figure 2.2: The effect of varying the length scale on the relative smoothness of functions. Draws from a GP as in Figure 2.1 with $\sigma = 2$ for 3 different lengthscales: $l = 0.02$ (left), $l = 0.2$ (center), $l = 1$ (right). Reproduced using code from https://www.pymc.io/.

2.3 USING GAUSSIAN PROCESSES TO INFER BINARY COMPACT-OBJECT MASS DISTRIBUTIONS

2.3.1 The BINNED GAUSSIAN PROCESS prior model

We use this section to define our BINNED GAUSSIAN PROCESS prior model for the distribution of compact binaries as a function of their component masses. In our specific study, we divide the two-dimensional (2-D) parameter space of binary component masses (m_1, m_2) into a number of bins ($N_{\rm bins}$) that are uniformly spaced in the log of the masses ($\log m_1 - \log m_2$). This method has been proposed in past literature in the context of exoplanet population inference as well as modeling the mass distribution of CBCs observed with LIGO-Virgo (Foreman-Mackey et al., 2014; Mandel et al., 2016). From an astrophysical perspective, since the masses span over a wide range ($1 - 100 M_\odot$ in this study) and over multiple binary sub-populations, working with the log of the masses is beneficial to modeling the distribution. We model the merger rate density across the 2-D mass bins i.e. $\frac{dN^{ab}}{\mathrm{d}\log m_1\,\mathrm{d}\log m_2\,\mathrm{d}V_C\,\mathrm{d}t_r}$, as a Gaussian process such that we have a constant rate density in a specific mass bin and one that is uniform in source co-moving volume (V_C) and source

time (t_r). We denote this by n^{ab} and mathematically this can be stated as,

$$\frac{dN^{ab}}{\mathrm{d}\,\log m_1\,\mathrm{d}\,\log m_2\,\mathrm{d}V_\mathrm{C}\,\mathrm{d}t_r} = \begin{cases} n^{ab}\,;\; M_a \,\leq m_1 \,\leq M_{a+1} \\ \text{and } M_b \,\leq m_2 \,\leq M_{b+1} \end{cases} \tag{2.4}$$

where $1 \leq$ a,b $\leq N_{\rm bins}$, $M_1 = M_{\rm min}$, $M_{N_{\rm bins}+1} = M_{\rm max}$. $M_{\rm min}$ and $M_{\rm max}$ are $1M_\odot$ and $100M_\odot$, respectively in this study. Note that since there is a degeneracy with respect to combinations of masses, we restrict our analyses below for binaries having $m_2 \leq m_1$ and then finally mirror our results about the $m_1 = m_2$ axis. Using just a single index (γ) to label the bins where $m_2 \leq m_1$, the rate densities can then be recast as,

$$\frac{dN^{\gamma}}{\mathrm{d}\,\log m_1\,\mathrm{d}\,\log m_2\,\mathrm{d}V_\mathrm{C}\,\mathrm{d}t_r} = n^{\gamma}. \tag{2.5}$$

Using such a definition for the binned merger rate density, the total merger rate density ($\mathcal{R}_{\rm total}$) of binaries across bins can be evaluated as,

$$\mathcal{R}_{\rm total} = \sum_{\gamma} n^{\gamma}\,\Delta log\, m_1^{\gamma}\,\Delta log\, m_2^{\gamma}. \tag{2.6}$$

One can also evaluate merger rate densities for specific sub-populations or set of bins by restricting the sum over γ in Eqn. 2.6 to the corresponding bins. The probability density distribution of the compact-binaries as a function of their masses and redshift can then be related to rate densities as,

$$\frac{dN^{\gamma}}{\mathrm{d}\,m_1 \mathrm{d}\,m_2 \mathrm{d}\,V_\mathrm{C} \mathrm{d}\,t_r}\frac{\mathrm{d}V_\mathrm{C}}{\mathrm{d}z}\frac{\mathrm{d}t_r}{\mathrm{d}t}\mathrm{d}t = \frac{n^{\gamma}}{m_1\,m_2}\frac{\mathrm{d}V_\mathrm{C}}{\mathrm{d}z}\frac{1}{1+z}\mathrm{d}t = N_{\rm tot}p^{\gamma}(m_1, m_2, z) \tag{2.7}$$

where we have used the relation between source-time (t_r), observer-time (t) and redshift (z) as $\frac{\mathrm{d}t_r}{\mathrm{d}t} = \frac{1}{1+z}$ and $N_{\rm tot}$ is the total number of merging compact binaries in the universe across masses and redshift.

The bin edges in the analyses presented in this chapter are located at $[1, 2, 2.5, 3, 4, 5, 6.5, 8, 10, 15, 20, 30, 40, 50, 60, 70, 80, 100]\, M_\odot$ with the assumption that $m_2 \leq m_1$. The probabilistic model for the logarithm of the rate density in each bin is defined as

$$\log n^\gamma \sim \mathcal{N}(\mu, \Sigma), \tag{2.8}$$

where μ is the mean $\log$ merger rate density in each bin and Σ is the covariance matrix that correlates the bins. Each element of the covariance matrix Σ is generated using a squared-exponential kernel $k(x, x')$ which is defined previously as,

$$k(x, x') = \sigma^2 \exp\left(\frac{-(x - x')^2}{2l^2}\right). \tag{2.9}$$

For the specific analysis here we take x, x' to be the bin centers in $\log m$. The parameter σ models the amplitude of the covariances while l is a parameter that defines the length scales over which bins are correlated. The prior distribution chosen here for the length scale is a log-normal distribution with a mean that is the average between the minimum bin spacing

$$\Delta_{\rm min} \equiv \min_{m_1, m_2} \Delta \log m, \tag{2.10}$$

and the maximum bin spacing

$$\Delta_{\rm max} \equiv \max_{m_1, m_2} \Delta \log m \tag{2.11}$$

with a standard deviation of $\frac{(\Delta_{\rm max} - \Delta_{\rm min})}{4}$. This constrains (at "2-σ" in the prior) the correlation length for the GP to lie between "one bin" and "all the bins." $\{\mu, \sigma, l \equiv \vec{\Lambda}\}$ are thus hyper-parameters that control the prior population distribution of coalescing compact binaries. For analyses presented in this chapter, Eqns. 2.10, 2.11 and the bin edges defined

Parameter	Description	Prior
μ	Mean $\log(\text{Rate})$ in each bin.	$\mathcal{N}(0, 10)$
σ	Amplitude of the covariance kernel.	$\mathcal{N}(0, 10)$
$\log(l)$	$\log(\text{Length scale})$ of the covariance kernel.	$\mathcal{N}(-0.085, 0.93)$

Table 2.1: Summary of BINNED GAUSSIAN PROCESS model parameters.

above give a mean and standard deviation of -0.085 and 0.93 respectively for such a log-normal distribution. The BINNED GAUSSIAN PROCESS model assumes a redshift distribution such that the overall merger rate of compact binaries is uniform-in-comoving volume. The spin distributions for each component are isotropic in direction and uniform in the spin magnitude with a maximum spin of 0.998 for black holes (BHs) and 0.4 for neutron stars (NSs); the prior distribution for the relevant parameters in Eqns. 2.8 and 2.9 is summarized in Table 2.1.

2.3.2 Posterior Derivation

In the previous sub-section, we have seen how the BINNED GAUSSIAN PROCESS model is used to construct a prior model for the merger rate density of compact-binaries as a function of their component masses. Here, we present a derivation of the posterior distribution of the bin-wise merger rate densities (n^{γ}) and hyper-parameters ($\vec{\Lambda}$) that define the mass distribution of compact-binaries. Before deriving the posterior , we state our notation here as follows:

1. i : Generic label for each event.

2. γ : Generic label for each two-dimensional component mass (m_1, m_2) bin.

3. $\{\vec{d^i}\}$: The set containing the observed data associated with each event. In our case here, these are the posterior estimate samples of the event-level parameters of the compact-binary such as its component masses (m_1, m_2) and redshift z.

4. $N_{\rm obs}$: The total number of observed astrophysical events.

5. $N_{\rm exp}$: The expected number of astrophysical events over the duration of the observation period, for a given set of population parameters $\equiv \{n^\gamma, \vec{\Lambda}\}$ and sensitivity of the GW detectors.

6. w^i_γ : Bin-weight associated with bin labeled γ corresponding to the (m_1, m_2) posterior samples for the i^{th} event.

7. $\langle V \rangle^\gamma T$: Monte-Carlo averaged bin-wise volume-time sensitivity of compact binaries.

We start generically from Bayes' formula for the posterior probability. Our target posterior distribution we want to find is that of the bin-wise merger rate densities and the hyper-parameters described in sub-section 2.3.1 - $\{\mu, \sigma, l \equiv \vec{\Lambda}\}$,

$$p(n^\gamma, \vec{\Lambda} | \, \{\vec{d^i}\}) \, = \frac{p(\{\vec{d^i}\} \, | \, n^\gamma, \vec{\Lambda}) \, p(n^\gamma, \vec{\Lambda})}{p(\{\vec{d^i}\})}. \tag{2.12}$$

As shown in sub-section 2.3.1, the prior distribution on n^γ is completely determined by the hyper-parameters. Also, the data $\{\vec{d^i}\}$ do not directly depend on these hyper-parameters. The posterior can then be written as,

$$p(n^\gamma, \vec{\Lambda} \, | \, \{\vec{d^i}\}) = \frac{p(\{\vec{d^i}\} | n^\gamma) \, p(n^\gamma | \vec{\Lambda}) \, p(\vec{\Lambda})}{p(\{\vec{d^i}\})} \tag{2.13}$$

where we have made use of the fact that $p(A, B) = p(A|B) \, p(B)$. The prior distributions are dictated by the distributions we assume for each parameter as given in Table 2.1 and the evidence $p(\{\vec{d^i}\})$ is a factor that does not qualitatively affect the posterior. It is a normalization that we can neglect. So, it is the population likelihood $p(\{\vec{d^i}\} | n^\gamma, N_{\rm exp})$ that

has a direct influence on our inference of the rate parameters. We thus focus on deriving an expression for the likelihood in what follows.

Our dataset $\{\vec{d^i}\}$ is a combined set of data for all the observed events ($N_{\rm obs}$) we consider in our analysis. Since the events are separated from each other by relatively large amounts of time [1] so as to not affect the data of another event in the set, we can assume the events to be independent and write the likelihood as a product over events. The population likelihood in gravitational-wave inference represents that for an in-homogeneous Poisson process and one can refer to a number of sources in the literature (Loredo, 2004; Farr et al., 2015a; Mandel et al., 2019a; Thrane & Talbot, 2019; Vitale et al., 2021) for a more in-depth derivation. Here we note that the merger-rate densities n^γ and hyper-parameters $\vec{\Lambda}$ are our population-level parameters of interest and $N_{\rm exp}$ is the expected number of astrophysical events for a given population model. As stated earlier, $N_{\rm exp}$ depends on the underlying population model and hence on n^γ. We will see in Section 2.3.3 how $N_{\rm exp}$ and n^γ are exactly related for the BGP model. For now we note this in the following equations by expressing this as $N_{\rm exp}(n^\gamma)$. The likelihood for such an in-homogeneous Poisson process is then given as,

$$p(\{\vec{d^i}\}|n^\gamma) = e^{-N_{\rm exp}(n^\gamma)} \prod_{i=1}^{N_{obs}} p(\vec{d^i}|n^\gamma). \tag{2.14}$$

With the availability of data for every observed event in our set, it is possible to perform Bayesian parameter estimation using a fiducial prior distribution $\pi(\vec{\theta})$ to determine the posterior distribution of the parameters $p(\vec{\theta}|\vec{d^i})$ for each event (Veitch et al., 2015a; Abbott et al., 2019a; The LIGO Scientific Collaboration et al., 2021a). Here $\vec{\theta}$ are the event-level parameters of the compact-binary such as its component masses (m_1, m_2) and red-

[1] Note : The typical duration of stellar-mass CBC signals in the sensitive frequency band of GW detectors is of $\mathcal{O}(seconds)$ to $\mathcal{O}(minutes)$.(Creighton & Anderson, 2011)

shift z. We can then write the likelihood as,

$$p(\{\vec{d^i}\}|n^\gamma) \propto e^{-N_{\rm exp}(n^\gamma)} \prod_{i=1}^{N_{\rm obs}} \int p(\vec{d^i}|\vec{\theta})\, p(\vec{\theta}|n^\gamma)\, {\rm d}\vec{\theta}. \tag{2.15}$$

In principle, determining the posterior distribution implies obtaining random samples or parameter estimates $\{m_1^i, m_2^i, z^i\}$ for each event using a fiducial prior distribution $\pi(m_1^i, m_2^i, z^i)$. We can then use Monte-Carlo importance sampling over the posterior samples to approximate the integral in Eqn. 2.15 as

$$p(\{\vec{d^i}\}|n^\gamma) \propto e^{-N_{\rm exp}(n^\gamma)} \prod_{i=1}^{N_{\rm obs}} \left\langle \frac{p(m_1^i, m_2^i, z^i|n^\gamma)}{\pi(m_1^i, m_2^i, z^i)} \right\rangle_i \tag{2.16}$$

where the $\left\langle ... \right\rangle_i$ denotes taking weighted averages over the posterior samples for the i^{th} event. From Eqn. 2.7 we note that $p(m_1^i, m_2^i, z^i|n^\gamma) \propto n^\gamma$. Combining all the other factors in that equation such as the product of masses, differential co-moving volume and the weighted prior $\pi(m_1^i, m_2^i, z^i)$ from parameter estimation, we can assign normalized posterior weights (w_i^γ) to each bin (γ) for each event (i),

$$w_i^\gamma = \sum_j \left(\frac{\delta^{\alpha_j \gamma}}{m_1^{i,j}\, m_2^{i,j}} \frac{{\rm d}V_{\rm C}}{{\rm d}z}\bigg|_{z^{i,j}} \frac{1}{1+z^{i,j}} \frac{1}{\pi(m_1^{i,j}, m_2^{i,j}, z^{i,j})} \right). \tag{2.17}$$

Here j is the index for each posterior sample for a given event (i) and δ is the Kronecker Delta Function. α_j denotes the 2-D bin in $m_1 - m_2$ to which the $j^{\rm th}$ posterior sample belongs. The weighted average in Eqn. 2.16 can then be written as a dot product between the weights (w_i^γ) and merger rate densities (n^γ),

$$p(\{\vec{d^i}\}|n^\gamma) \propto e^{-N_{\rm exp}(n^\gamma)} \prod_{i=1}^{N_{\rm obs}} \left(\sum_\gamma w_i^\gamma n^\gamma \right). \tag{2.18}$$

Combining Eqns. 2.13 and 2.18 we get our target posterior as:

$$p(n^\gamma, \vec{\Lambda} \,|\, \{\vec{d^i}\}) \propto \; e^{-\,N_{\rm exp}(n^\gamma)} \prod_{i=1}^{N_{\rm obs}} \Big(\sum_\gamma w_i^\gamma n^\gamma \Big) \, p(n^\gamma|\vec{\Lambda}) \, p(\vec{\Lambda}). \tag{2.19}$$

2.3.3 Selection Effects or the Malmquist Bias in GW Population Inference

The other important variable in Eqn. 2.19 is the expected number of astrophysical signals in the data i.e. $N_{\rm exp}$. $N_{\rm exp}$ reflects the fact that there are selection effects that are present in gravitational-wave population inference (Abbott et al., 2016a; Fishbach et al., 2018; Mandel et al., 2019a). That is, there are biases in the detection of compact-binaries by GW detectors based on their parameters such as masses, spins and redshifts. For example, binaries with higher component masses have a higher amplitude for their GW signal and can be detected out to higher redshifts compared to binaries with low mass. Such a bias in astronomy is termed as a Malmquist bias (Malmquist, 1922, 1925). Intrinsically, $N_{\rm exp}$ depends on the merger rate densities n^γ and thereby on the population model hyper-parameters. It is defined as follows - say we have population-level hyper-parameters $\vec{\Lambda}$, event-level parameters $\vec{\theta}$ and observed data $\vec{d}$. We further assume that it is possible to assign every signal in the data with a detection statistic ρ (such as for example the false alarm rate or signal to noise ratio). The detection statistic is a function of the data ($f(\vec{d})$) that helps construct the catalog of observed signals by determining which signals are detectable based on a defined threshold detection statistic $\rho_{\rm thr}$. For the results presented in this chapter, our chosen detection statistic threshold is a false alarm rate of 1 per 4 years.

In our population inference we are interested in the cases where the detection statistic is above threshold and we want to know that for a given set of event-level parameters $\vec{\theta}$ what is the probability that the signal from such a system is detectable? In the absence of noise, the answer to this question is straight-forward but in reality it depends on the data since every realization of the data corresponds to a different noise realization. We

can write:

$$p(\rho \geq \rho_{\rm thr}|\vec{\theta}) = \int \mathrm{d}\vec{d}\, p(\rho \geq \rho_{\rm thr}|\vec{d},\vec{\theta})\, p(\vec{d}|\vec{\theta}). \tag{2.20}$$

We can see that when $f(\vec{d}) \geq \rho_{\rm thr}$ ($f(\vec{d}) < \rho_{\rm thr}$), $p(\rho \geq \rho_{\rm thr}|\vec{d},\vec{\theta}) = 1\,(0)$. Thus,

$$p(\rho \geq \rho_{\rm thr}|\vec{\theta}) = \int\limits_{f(\vec{d})>\rho_{\rm thr}} \mathrm{d}\vec{d}\, p(\vec{d}|\vec{\theta}). \tag{2.21}$$

Then the expected number of signals in the data for a given population defined by hyper-parameters $\vec{\Lambda}$ is,

$$N_{\rm exp} = \int \mathrm{d}\vec{\theta}\, \frac{\mathrm{d}N}{\mathrm{d}\vec{\theta}}(\vec{\Lambda})\, p(\rho \geq \rho_{\rm thr}|\vec{\theta}). \tag{2.22}$$

Making the connection with Eqn. 2.7 we see that for our case here — $\frac{\mathrm{d}N}{\mathrm{d}\vec{\theta}}(\vec{\Lambda}) \equiv \frac{dN}{\mathrm{d}\,m_1 \mathrm{d}\,m_2 \mathrm{d}\,z}(n^\gamma)$ which can be related to the merger rate densities n^γ to give

$$N_{\rm exp} = \int \mathrm{d}m_1\, \mathrm{d}m_2\, \mathrm{d}z\, \mathrm{d}t \frac{n^\gamma}{m_1\, m_2} \frac{\mathrm{d}V_{\rm C}}{\mathrm{d}z} \frac{1}{1+z} p(\rho \geq \rho_{\rm thr}|m_1, m_2, z). \tag{2.23}$$

In GW population inference, equations such as Eqn. 2.23 are estimated by Monte-Carlo importance sampling (Tiwari, 2018) since finding the detection probability $p(\rho \geq \rho_{\rm thr}|m_1, m_2, z)$ analytically is not tractable. In this method, a large suite of simulated signals (also called injections) are introduced into the observed GW data. The simulated signals are drawn from a population distribution $p_{\rm inj}(\vec{\theta})$ that provides compact binaries over a relatively broad section of the expected parameter space of the event-level parameters $\vec{\theta}$. The simulated GW data stream is then analyzed by detection pipelines to see how many injections are above the same detection threshold $\rho_{\rm thr}$ chosen to construct the actual catalog of astrophysical signals. The full description of the simulated distributions used to construct the

results presented in this chapter are available at The LIGO Scientific Collaboration et al. (2021b). Assuming that we have $\mathrm{N_{found}}$ injections that are detected above the threshold out of a total number of $\mathrm{N_{inj}}$ injections, Eqn. 2.22 can be estimated as:

$$N_{\rm exp} = \frac{1}{\mathrm{N_{inj}}} \sum_{i=0}^{\mathrm{N_{found}}} \frac{\mathrm{d}N}{\mathrm{d}\vec{\theta^i}}(\vec{\Lambda}) \frac{1}{p_{\rm inj}(\vec{\theta^i})}. \tag{2.24}$$

Using this in Eqn. 2.23, we can see that each found injection will contribute to a unique bin and we can write the expected number of signals as:

$$N_{\rm exp} = \frac{1}{\mathrm{N_{inj}}} \sum_{i=0}^{\mathrm{N_{found}}} \sum_{\gamma} \frac{\delta^{\alpha_i \gamma} n^{\gamma}}{m_1^i\, m_2^i} \frac{\mathrm{d}V_{\rm C}}{\mathrm{d}z}\bigg|_{z^i} \frac{T}{1+z^i} \frac{1}{p_{\rm inj}(m_1^i,\, m_2^i,\, z^i)}. \tag{2.25}$$

where δ is the Kronecker Delta Function and α_i denotes the 2-D bin in $m_1 - m_2$ to which the $i^{\rm th}$ injection belongs. T is the total time in the observer or detector frame during which the signals have the potential to be detected. We can simplify this equation and re-write it as,

$$N_{\rm exp} = \sum_{\gamma} n^{\gamma} \left\langle V \right\rangle^{\gamma} T\, \Delta log\, m_1^{\gamma}\, \Delta log\, m_2^{\gamma} \tag{2.26}$$

by making the connection,

$$\left\langle V \right\rangle^{\gamma} = \frac{1}{\Delta log\, m_1^{\gamma}\, \Delta log\, m_2^{\gamma}} \sum_{i=0}^{\mathrm{N_{found}}} \frac{\delta^{\alpha_i \gamma}}{m_1^i\, m_2^i} \frac{\mathrm{d}V_{\rm C}}{\mathrm{d}z}\bigg|_{z^i} \frac{1}{1+z^i} \frac{1}{p_{\rm inj}(m_1^i,\, m_2^i,\, z^i)}. \tag{2.27}$$

$\left\langle V \right\rangle^{\gamma}$ is the comoving-volume within which the injections in bin γ are detectable assuming they come from a population defined by the merger rate densities n^{γ} and hyper-parameters $\{\mu, \sigma, l \equiv \vec{\Lambda}\}$. In other words, this excludes periods of time when the detectors are not operational or when there exists glitches in the data.

Using Eqns. 2.8, 2.19 and 2.26 we sample our posterior using Markov Chain Monte

Carlo (MCMC) methods and routines in the Gaussian process modules described in `PyMC3` (Salvatier et al., 2016) and infer the posterior distributions which form the basis of our results in the following section. As is standard with MCMC methods, we sample the logarithm of the posterior distribution which can be written in its expanded form as,

$$\begin{aligned}\log(p(n^\gamma, \mu, \sigma, l|\,\{\vec{d^i}\})) \quad \propto \quad & \sum_{i=0}^{N_{\rm obs}} \log(\sum_\gamma w_i^\gamma n^\gamma) - (\log n^\gamma - \mu)\Sigma^{-1}(\log n^\gamma - \mu)^T - \log n^\gamma - \frac{\log|\Sigma|}{2} \\ & -\frac{1}{2}\frac{\mu^2}{10^2} - \frac{1}{2}\frac{\sigma^2}{10^2} - \frac{1}{2}\frac{(\log l + 0.085)^2}{0.93^2} - N_{\rm exp}(n^\gamma) \end{aligned} \tag{2.28}$$

where Σ^{-1} and $|\Sigma|$ are the inverse and determinants respectively, of the covariance matrix Σ defined in Section 2.3.1 for the the BGP model.

2.4 RESULTS

In this section, we present our results of using the BGP model described in Section 2.3 to infer the mass distribution of merging compact binaries. These results are based on data from gravitational-waves detected through the third observing run of Advanced LIGO-Virgo and which form the cumulative Gravitational Wave Transient Catalog 3 (GWTC-3) (The LIGO Scientific Collaboration et al., 2021a). As stated previously, we consider events which satisfy having a false alarm rate of less than 1 per 4 years. At this threshold, the catalog contains 67 events which are listed in Table I of Abbott et al. (2021a).

2.4.1 Binary Merger Population Across All Masses

The feature of the BGP model is that it is independent of any parameters that depend on the masses of the binary (for example, mass-dependent power laws with specific limits for the minimum and maximum component masses). This allows us to analyze the

population of compact-binaries over the entire range of binaries spanning NSs and BHs.

Figure 2.3 shows the inferred median merger rate density, in each of the 2-D bins defined in Section 2.3.1, using data from GWTC-3. There is a clear distinction in the sub-populations between binary neutron stars (BNSs), neutron star–black holes (NSBHs) and binary black holes (BBHs). One of the important features to note is the appearance of structure in the BBH population with pronounced peaks where primary masses (mass of the heavier component in the binary) are around $10M_{\odot}$ and $35M_{\odot}$. We will further describe this structure in more detail in Section 2.4.2 with an emphasis on the primary component mass of the binary. Resolving structure in the BNS and NSBH populations is both challenging and statistically insignificant at this stage of the catalog. This is owing to the relatively smaller number of events contributing to the relevant bins and also due to the fact that the bin scale at these masses limits the ability to capture the variability in these sub-populations. As is expected, our inferred NSBH populations seem to be representative of the observed events (GW200105 and GW200115; refer Table I of Abbott et al. (2021a)) driving the inference in the corresponding bins. The inferred BNS population is primarily driven by parameter estimates from the two significant BNS events — GW170817 and GW190425 (refer Table I of Abbott et al. (2021a)).

Following Eqn. 2.6, we can compute inferred merger rate densities for various sub-populations in the 2-D parameter space of component masses using the BGP model. Table 2.2 shows the inferred merger rate densities in the various mass bins defined in Section 2.3.1 for different population models used in Abbott et al. (2021a) that analyse the binary population across the entire mass spectrum — POWER LAW + DIP + BREAK (PDB), MULTI SOURCE (MS) and BGP. These results update the binary merger rate densities from previous studies (Abbott et al., 2021e) using previous catalogs (Abbott et al., 2021b). In particular, NSBH rate densities obtained by modeling the mass distribution in this

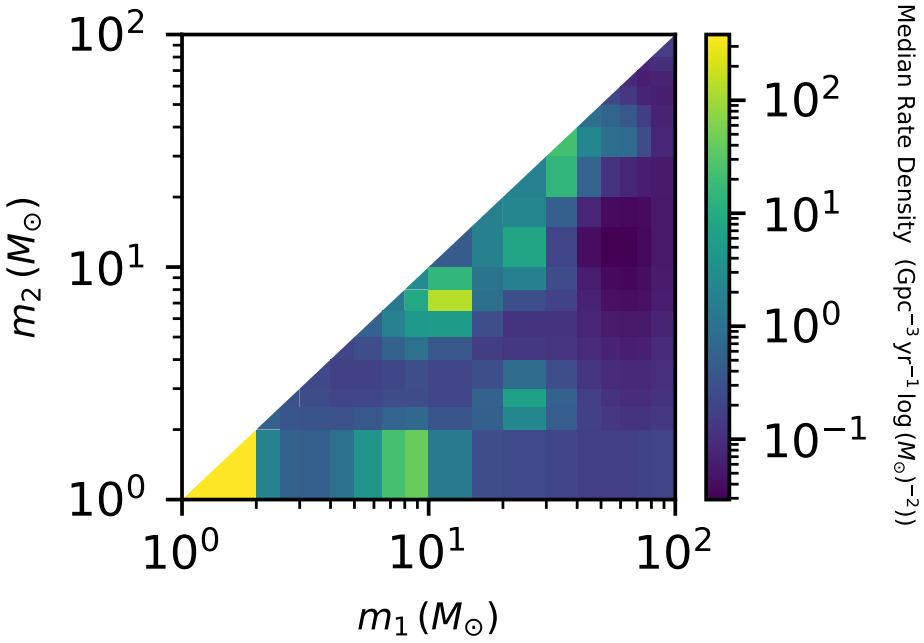

Figure 2.3: Binned median merger rate density inferred using the BGP model with a false alarm rate threshold of $< 0.25\mathrm{yr}^{-1}$. The bins span component masses from 1 to $100M_\odot$

relevant parameter space are quoted for the first time with the BGP model inferring rate densities $\mathcal{R}_{\mathrm{NSBH}} = 32.0^{+62.0}_{-24.0}\,\mathrm{Gpc}^{-3}\mathrm{yr}^{-1}$.

Another feature that can be derived from the sub-structure observed, is the impact of asymmetric binaries on the primary mass distribution. Figure 2.4 illustrates how off-diagonal bins dominate the merger rate across most the primary mass axis. This indicates that the contribution of asymmetric mergers like NSBHs to the marginal distribution over primary mass is important.

Figure 2.5 shows the consistency of the BGP model in analyzing binaries with NS-scale masses, with other parametric models — MULTI SOURCE (MS) and POWER LAW + DIP + BREAK (PDB) - of the compact binary population across masses. Details of these models

	BNS	NSBH	BBH	NS-Gap	BBH-gap	Full
	$m_1 \in [1, 2.5]M_\odot$	$m_1 \in [2.5, 50]M_\odot$	$m_1 \in [2.5, 100]M_\odot$	$m_1 \in [2.5, 5]M_\odot$	$m_1 \in [2.5, 100]M_\odot$	$m_1 \in [1, 100]M_\odot$
	$m_2 \in [1, 2.5]M_\odot$	$m_2 \in [1, 2.5]M_\odot$	$m_2 \in [2.5, 100]M_\odot$	$m_2 \in [1, 2.5]M_\odot$	$m_2 \in [2.5, 5]M_\odot$	$m_2 \in [1, 100]M_\odot$
PDB (pair)	170^{+270}_{-120}	27^{+31}_{-17}	$25^{+10}_{-7.0}$	19^{+28}_{-13}	$9.3^{+15.7}_{-7.2}$	240^{+270}_{-140}
PDB (ind)	44^{+96}_{-34}	73^{+67}_{-37}	$22^{+8.0}_{-6.0}$	$12^{+18}_{-9.0}$	$9.7^{+11.3}_{-7.0}$	150^{+170}_{-71}
MS	660^{+1040}_{-530}	49^{+91}_{-38}	37^{+24}_{-13}	$3.7^{+35.3}_{-3.4}$	$0.12^{+24.88}_{-0.12}$	770^{+1030}_{-530}
BGP	$98.0^{+260.0}_{-85.0}$	$32.0^{+62.0}_{-24.0}$	$33.0^{+16.0}_{-10.0}$	$1.7^{+30.0}_{-1.7}$	$5.2^{+12.0}_{-4.1}$	$180.0^{+270.0}_{-110.0}$

Table 2.2: Reproduced using the public data release (LIGO Scientific Collaboration et al., 2021) for Abbott et al. (2021a). Merger rate densities in $\mathrm{Gpc}^{-3}\mathrm{yr}^{-1}$ for different component mass ranges (defined by the ranges in m_1 and m_2) across different population models, quoted at the 90% credible interval. For details regrading models other than BGP refer to Abbott et al. (2021a).

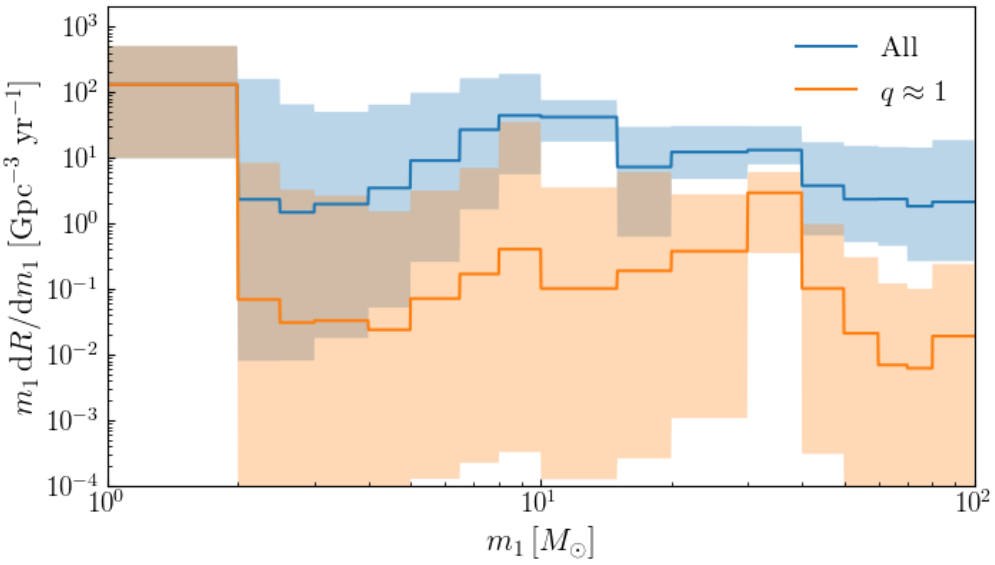

Figure 2.4: Reproduced using the public data release (LIGO Scientific Collaboration et al., 2021) for Abbott et al. (2021a). Differential merger rate computed using the BGP model as a function of primary mass across all mass bins and contrasted with that when considering only the diagonal $q \simeq 1$ bins in Fig. 2.3. Solid curves represent the median rate densities and shaded areas denote 90% credible regions.

are given in Abbott et al. (2021a). Different models with different assumptions for the population shape appear to statistically agree on the differential merger rate. Nonetheless, these results also highlight the importance of modeling systematics when analyzing objects with NS-scale masses.

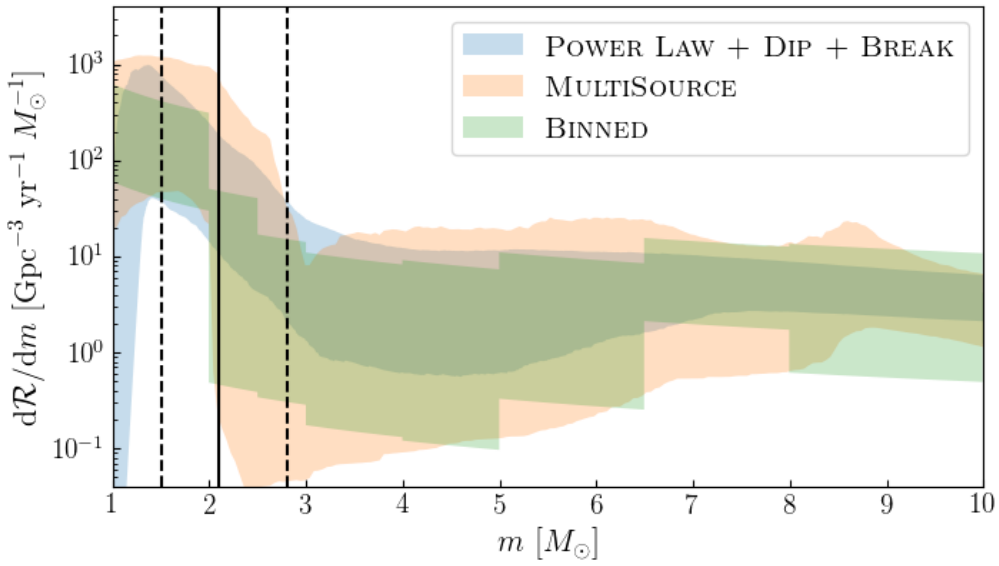

Figure 2.5: Reproduced using the public data release (LIGO Scientific Collaboration et al., 2021) for Abbott et al. (2021a). Differential merger rate as a function of component mass for the BGP model and compared with the PDB and MS models defined in Abbott et al. (2021a). Shaded areas denote 90% credible regions; vertical black lines denote the median (solid) and 90% credible intervals (dashed) of the lower boundary of the mass gap, $M_{\mathrm{gap}}^{\mathrm{low}}$, in the PDB model.

2.4.2 Binary Black Hole Population

We now turn our focus to the BBH population and, in particular, look at the primary mass distribution of binaries inferred using the BGP model. The one-dimensional distribution in m_1 here is derived by marginalizing the posterior support over the appropriate bins in the m_2 dimension. As seen in Figure 2.6, several models including the BINNED GAUSSIAN PROCESS construct the inferred primary mass distribution. For details regarding other models shown in the figure, refer to Abbott et al. (2021a). There are several interesting features in the BBH mass spectrum. Notably, across all models the mass function is inferred to peak globally at $\sim 10M_\odot$. Such a peak and its relative height can inform formation channels for BBHs as noted in Section 2.5. Additionally, the secondary local peak at $\sim 35M_\odot$ is another feature that models seem to agree on. Evidence for such a peak has

	$m_1 \in [5, 20]M_\odot$ $m_2 \in [5, 20]M_\odot$	$m_1 \in [20, 50]M_\odot$ $m_2 \in [5, 50]M_\odot$	$m_1 \in [50, 100]M_\odot$ $m_2 \in [5, 100]M_\odot$	All BBH
PP	$23.6^{+13.7}_{-9.0}$	$4.5^{+1.7}_{-1.3}$	$0.2^{+0.1}_{-0.1}$	$28.3^{+13.9}_{-9.1}$
BGP	$20.0^{+11.0}_{-8.0}$	$6.3^{+3.0}_{-2.2}$	$0.75^{+1.1}_{-0.46}$	$33.0^{+16.0}_{-10.0}$
FM	$21.1^{+11.6}_{-7.8}$	$4.3^{+2.0}_{-1.4}$	$0.2^{+0.2}_{-0.1}$	$26.5^{+11.7}_{-8.6}$
PS	$27^{+12}_{-8.8}$	$3.5^{+1.5}_{-1.1}$	$0.19^{+0.16}_{-0.09}$	$31^{+13}_{-9.2}$

Table 2.3: Reproduced using the public data release (LIGO Scientific Collaboration et al., 2021) for Abbott et al. (2021a). Merger rates by different models from Abbott et al. (2021a) in $\mathrm{Gpc}^{-3}\mathrm{yr}^{-1}$ for the mass ranges encompassing BBH binaries; quoted at the 90% credible interval. There is broad agreement among models depsite major differences in modeling assumptions.

also been presented previously (Abbott et al., 2021e) however its statistical significance is higher with the latest GW catalog. Another feature is the absence of a steep decline in the mass distribution beyond $\sim 45M_\odot$. This result challenges massive stellar evolution models and, as noted later, might suggest a different formation channel for these massive black holes.

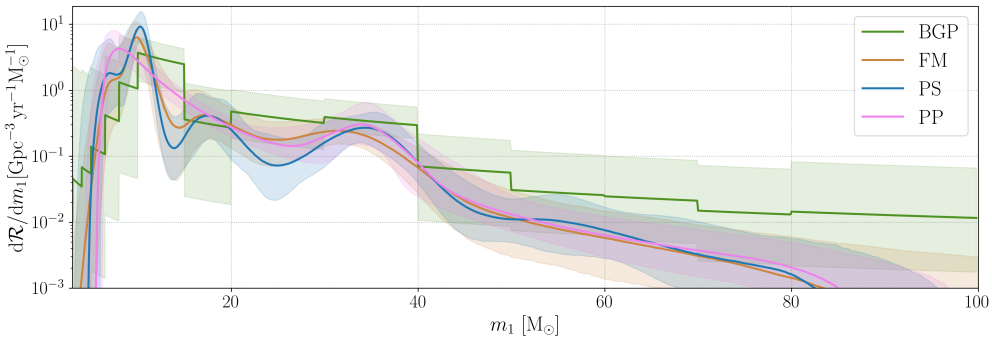

Figure 2.6: Reproduced using the public data release (LIGO Scientific Collaboration et al., 2021) for Abbott et al. (2021a). The differential merger rate density for the primary mass predicted using three semi-parametric models and the parametric POWER LAW + PEAK model for events passing a false alarm rate threshold of $< 0.25\mathrm{yr}^{-1}$. . Solid curves are the medians and the colored bands are the 90% credible intervals. All models infer a local maximum in the merger rate at around $10M_\odot$ and $35M_\odot$.

2.5 DISCUSSION

In this chapter, we presented a model based on previous work in Foreman-Mackey et al. (2014); Mandel et al. (2016), that can be used to infer the mass distribution of compact binaries using data from gravitational-wave catalogs such as GWTC-3 (The LIGO Scientific Collaboration et al., 2021a). The key feature of this model is that it is independent of any physical parameters that define the binary system and makes no apriori assumptions about the shape of the target distribution. Instead, as described in Section 2.3.1 the model makes use of a Gaussian process defined across a grid of bins in the 2-D parameter space of the component masses of the binary.

Based on data from GWTC-3, we presented the results of our hierarchical Bayesian inference to derive the posterior distributions on the hyper-parameters defining the BGP model and thereby construct the population of compact binaries. The results from the BGP model highlight the ability to analyze all binary sub-populations (including BNS, NSBH and BBH) within the same formalism. The inference results presented in Section 2.4.1 indicate statistically significant structure in the BBH population which cannot be modeled using a simple function such as single power-law. This has interesting implications for astrophysics as it can shed light on the processes and channels of binary formation and evolution (Stevenson et al., 2015; Fishbach et al., 2017; Barrett et al., 2018; Wysocki et al., 2018; Yang et al., 2019; Doctor et al., 2020; McKernan et al., 2020; Zevin et al., 2021; Wong et al., 2021; Romero-Shaw et al., 2021). In particular, the inferred peak at $\sim 10 M_{\odot}$ in Figure 2.6 can help inform which of the formation channels such as isolated binaries (Belczynski et al., 2016a; Giacobbo & Mapelli, 2018; Wiktorowicz et al., 2019; Belczynski et al., 2020), globular clusters (Kulkarni et al., 1993; Rodriguez et al., 2015, 2016; Askar et al., 2018; Hong et al., 2018; Banerjee, 2022) or galactic nuclei (Antonini & Rasio, 2016; Hoang et al., 2018; Fragione et al., 2019; Ford & McKernan, 2021) is the dominant

contributor to the mergers observed by LIGO-Virgo (Abbott et al., 2021a).

Furthermore, another feature observed from Figure 2.6 is the non-zero probability for the existence of BHs with primary masses greater than $\sim 40M_{\odot}$. Current stellar evolution models predict a lack of BHs in the mass range $\sim 40 - 120M_{\odot}$ owing to pair-instability supernova processes in massive stellar cores (Belczynski et al., 2016b; Woosley, 2017; Marchant et al., 2019; Stevenson et al., 2019; Woosley & Heger, 2021). Thus, the inferred results here indicate either the need to update our models for evolution with respect to massive stars or the need to incorporate dynamical processes such as hierarchical mergers (Doctor et al., 2020) or accretion (Inayoshi et al., 2016; Safarzadeh & Haiman, 2020; van Son et al., 2020) to explain the existence of these higher mass BHs. Additionally, the peak observed at $\sim 35M_{\odot}$ might indicate an excess of BHs formed from the collapse of massive stellar cores owing to pulsational pair-instability supernovae (Talbot & Thrane, 2018; Stevenson et al., 2019) or a different sub-population of binary BHs with formation channels that are different from those that produce other binaries.

In demonstrating our results across Sections 2.4.1 and 2.4.2, we compared the results of the BGP model to those from other models (parametric and semi-parametric) introduced in Abbott et al. (2021a). Our results, including the shape of the mass distribution as well as merger rate densities shown in Tables 2.2 and 2.3, are statistically consistent with other models.

The BGP model however, has limitations that can be improved for future analyses. A more practical model would be one that allows the population to vary with all the physical parameters of the binary including redshift and spin as opposed to only the masses. This would enable GW detections to inform us about important correlations that exist between these parameters in the population. The redshift model we assumed for the merger rate density was one that does not evolve or is uniform as a function of the co-moving vol-

ume. Current analyses have already begun placing interesting constraints on the redshift evolution of the merger rate and, in fact, find the merger rate density to be increasing as function of redshift (Abbott et al., 2021e,a). Also, studies are finding correlations between the mass and spin parameters of BBHs (Abbott et al., 2021a; Callister et al., 2021). Further, the analysis presented in this chapter used a number of discrete bins in each dimension of m_1 and m_2 for the BINNED GAUSSIAN PROCESS. In order to resolve structures with future catalogs of GW events, especially in the BNS and NSBH sub-populations, the number of bins would need to be increased. Although this might increase the computational complexity of the method, the trade-off in discerning interesting features in the population cannot be ignored.

With the increasing sensitivity of GW detectors in the future, we are entering an era where a significantly larger number of GW events will inform the population of compact binaries and constrain fundamental astrophysical processes (Punturo et al., 2010; Abbott et al., 2017a, 2020c; Kalogera et al., 2019). Such large catalogs of GW events will need flexible modeling methods such as those demonstrated here in order to infer features in the population that cannot be modeled by simple functions.

CHAPTER 3

Inferring kilonova population properties with a hierarchical Bayesian framework I : Non-detection methodology and single-event analyses

3.1 INTRODUCTION

Mergers of neutron stars and neutron star-black hole binaries (BNS and NSBH) present unique opportunities to probe multi-messenger astrophysics (e.g., Metzger, 2019). While they are among the best sources of gravitational-wave (GW) emission detectable by GW observatories (Abbott et al., 2019b, 2020b) such as Advanced LIGO and Advanced Virgo (Aasi et al., 2015; Acernese et al., 2015), their potential detection in the electromagnetic (EM) spectrum by surveys around the world represents one of the most challenging searches for astrophysical transients. During the merger, significant amounts of neutron-star (NS) matter are ejected at sub-relativistic speeds due to either tidal or hydrodynamical forces; the radioactive decay of r-process elements synthesized in the neutron-rich merger ejecta powers a thermal ultraviolet, optical and near infrared transient, often referred to as a kilonova (KN) (Li & Paczyński, 1998; Rosswog, 2005; Metzger et al.,

2010; Tanaka & Hotokezaka, 2013). Despite their color- and luminosity-evolution being viewing-angle dependent (Kasen et al., 2015; Bulla, 2019; Kawaguchi et al., 2020; Korobkin et al., 2020; Zhu et al., 2021), their (largely) isotropic emission makes KNe one of the promising targets for EM counterpart follow-up observations (Roberts et al., 2011). However, they can be short-lived, faint, and peak in the infrared, making detection difficult (Kasen et al., 2015; Tanaka, 2016; Barnes et al., 2016; Metzger, 2019; Nakar, 2019).

From an observational standpoint, the GW detection of the BNS merger GW170817 (Abbott et al., 2017b) provided the first, and only, multi-messenger follow-up of a GW event to yield an associated KN (AT2017gfo) to date (Abbott et al., 2017c). Observations were recorded in the ultraviolet, optical and near-infrared (Andreoni et al., 2017; Chornock et al., 2017; Coulter et al., 2017; Cowperthwaite et al., 2017; Drout et al., 2017; Evans et al., 2017; Kasliwal et al., 2017, 2019a; Kilpatrick et al., 2017; Lipunov et al., 2017; McCully et al., 2017; Nicholl et al., 2017; Shappee et al., 2017; Soares-Santos et al., 2017; Pian et al., 2017; Smartt et al., 2017; Tanvir et al., 2017; Utsumi et al., 2017). These observations have highlighted the ability to test models of KNe and provide constraints on the ejecta mass and velocity (Abbott et al., 2017d; Cowperthwaite et al., 2017; Perego et al., 2017; Pian et al., 2017; Smartt et al., 2017; Tanaka et al., 2017; Waxman et al., 2018; Coughlin et al., 2019b; Kawaguchi et al., 2020; Heinzel et al., 2021; Raaijmakers et al., 2021), r-process elemental abundances (Côté et al., 2018; Hotokezaka et al., 2018; Radice et al., 2018; Tanaka et al., 2018; Hotokezaka & Nakar, 2020; Siegel, 2019), the NS equation of state (Foucart et al., 2018; Coughlin et al., 2018b; Radice & Dai, 2019; Hinderer et al., 2019; Breschi et al., 2021; Nicholl et al., 2021) and Hubble Constant (Hotokezaka et al., 2019; Dietrich et al., 2020; Dhawan et al., 2020).

There are a plethora of studies in the literature that model the luminosity evolution of KNe (Kasen et al. 2017; Coughlin et al. 2018b; Wollaeger et al. 2018; Bulla 2019; Kawaguchi

et al. 2020; also see references in Metzger 2019). Despite the detection of the KN from GW170817, there are significant uncertainties in the model parameter space (Barnes et al., 2016; Rosswog et al., 2017; Zhu et al., 2018; Kasliwal et al., 2019a; Wu et al., 2019; Heinzel et al., 2021). These uncertainties primarily stem from the range of ejecta masses expected from such mergers and the content of nuclear matter assumed in the models (Barnes et al., 2020; Foucart et al., 2021; Kullmann et al., 2021; Just et al., 2021). While uncertainties in the mass ejected from BNS systems have been shown to be driven mostly by the total mass and mass ratio of the system (Bauswein et al., 2013; Hotokezaka et al., 2013; Köppel et al., 2019; Kiuchi et al., 2019), those in models for NSBH systems are influenced by the mass ratio, BH spin and NS radius (Etienne et al., 2009; Kyutoku et al., 2015; Kawaguchi et al., 2016; Foucart et al., 2018; Zhu et al., 2020).

The third observing run of Advanced LIGO and Virgo (O3[1]), which lasted 11 months, yielded a total of 15 publicly announced NSBH and BNS candidates. Several teams, including Global Relay of Observatories Watching Transients Happen (GROWTH; Kasliwal et al. 2020), Electromagnetic counterparts of gravitational wave sources at the Very Large Telescope (ENGRAVE; Levan 2020), Global Rapid Advanced Network Devoted to the Multi-messenger Addicts (GRANDMA; Antier, S. and Agayeva, S. and AlMualla, M. and others 2020), Gravitational-wave Optical Transient Observer (GOTO; Gompertz et al. 2020), All Sky Automated Survey for SuperNovae (ASAS-SN; de Jaeger et al. 2021), Asteroid Terrestrial Last Alert System (ATLAS; Tonry et al. 2018), Panoramic Survey Telescope and Rapid Response System (Pan-STARRS; Chambers et al. 2016), MASTER-Net (Lipunov et al., 2017), Dark Energy Survey Gravitational Wave Collaboration (DES-GW; Soares-Santos et al. 2017) and Japanese collaboration for Gravitational wave ElectroMagnetic follow-up (J-GEM; Sasada et al. 2021) conducted wide-field searches within the

[1] https://gracedb.ligo.org/superevents/public/O3/

skymaps of BNS and NSBH candidates and pursued follow-up of interesting transient candidates found therein, but no plausible EM counterparts were found (e.g., Coughlin et al. 2019c).

Nevertheless, the apparent dearth of counterparts during all of O3 can illuminate our understanding of the intrinsic properties of KNe. On an individual GW event basis, observational upper limits can be used to constrain the KN emission from a potentially associated counterpart and infer properties of the binary (Hosseinzadeh et al., 2019; Andreoni et al., 2020; Anand et al., 2020; Morgan et al., 2020). Other works, e.g., Coughlin et al. (2019c); Lundquist et al. (2019a); Gompertz et al. (2020); Antier, S. and Agayeva, S. and AlMualla, M. and others (2020); Kasliwal et al. (2020), have demonstrated ways to synthesize survey observations for a suite of GW events to constrain the KN population as a whole. In particular, Kasliwal et al. (2020) formulated a method for constraining the luminosity function of the KN population. Assuming a non-uniform distribution of KN initial luminosities between -10 and -20 absolute magnitude, their findings suggest that no more than 57% (89%) of KNe could be brighter than -16.6 mag assuming flat (fading at 1 mag day^{-1}) evolution (Kasliwal et al., 2020).

In this paper, we present `nimbus`(Mohite, 2021): a hierarchical Bayesian framework to infer the intrinsic luminosity parameters of the population of KNe associated with GW events, based purely on non-detections. Key features of this framework include the simultaneous use of probabilistic source distance information from GW observations and corresponding upper limits from EM surveys, accounting for the fraction of the skymap searched by a given survey for each event, self-consistent inclusion of the probability of a GW event being of astrophysical origin ($p_{\rm astro}$) and the ability to model multi-band luminosity evolution. The framework is agnostic to the specific luminosity model used and thus can be used to constrain a wide variety of models in the literature.

As a first example and proof of concept, we demonstrate realistic constraints possible on the KN emission from the past follow-up of the event GW190425 (Abbott et al., 2020a) conducted with the Zwicky Transient Facility (ZTF) (Coughlin et al., 2019d). ZTF is an optical time-domain survey, consisting of a CCD camera with a 47 deg^2 field-of-view installed on the 48-inch Samuel Oschin Schmidt Telescope at the Palomar Observatory. Scanning the sky at an areal survey speed of $\sim$3750 square degrees per hour in three custom filters, ZTF-g, ZTF-r, ZTF-i; it reaches a median depth of 20.4 mag in 30 s exposures in its nominal nightly survey but can also conduct deeper target-of-opportunity followup of external events (Coughlin et al., 2019a); for a comprehensive review of the ZTF instrument, software, and survey see Bellm et al. (2019); Masci et al. (2019); Graham et al. (2019); Dekany et al. (2020).

Among the 13 events searched by ZTF in Advanced LIGO's third observing run (Kasliwal et al., 2020) that could have a probable EM counterpart, based on the probability of the system containing a NS i.e. p(BNS) or p(NSBH), GW190425 is so far the only significant binary merger event confirmed by LIGO and Virgo (Abbott et al., 2020a) to likely be a BNS based on the posterior inference of its masses; therefore, our analysis herein focuses on this event alone. GW190425 was located at a distance of 159^{+69}_{-71} Mpc and its final 90% credible localization spanned 8284 deg^2 (Abbott et al., 2020a). For GW190425, ZTF observed $\sim$8000 deg^2, corresponding to 45% probability of the initial BAYESTAR skymap (Singer & Price, 2016) which reduced to 21% integrated probability within the 90% credible region of the LALInference skymap (Veitch et al., 2015b) and attained a median depth of m$_{AB}$ $\approx$21 mag in g- and r-bands (Coughlin et al., 2019a). For the purpose of this analysis, we consider ZTF areal coverage within the entire LALInference skymap, which corresponds to 32% probability. No KN was identified in the observed region of this event by ZTF or other optical telescopes (Lipunov et al., 2019; Lundquist et al., 2019b; De et al.,

2019; Xu et al., 2019; Kasliwal et al., 2019b; McBrien et al., 2019; Smith et al., 2019; Steeghs et al., 2019; Blazek et al., 2019; Li et al., 2019), or for any other GW event followed-up with ZTF (Kasliwal et al., 2020).

This paper is organized as follows. In Sec. 3.2, we provide a detailed description of the Bayesian framework including a derivation of the model posterior and important aspects that impact the inference. We then present our main inference results on GW190425 using two different prior assumptions in Sec. 3.3. We also use this Section to compare our results with those obtained from `simsurvey` (Feindt et al., 2019), a simulation tool for astronomical surveys previously used in the literature to constrain KN luminosity distributions (Kasliwal et al., 2020). We then conclude with a discussion of our results and future outlook in Sec. 3.4.

3.2 BAYESIAN FRAMEWORK

In order to derive constraints on KN parameters, we make use of a hierarchical Bayesian statistical framework. Our goal is to find the posterior probability distribution of the parameters of interest $\vec{\theta}$, given the data $\{d^i\}$. The derivation here follows analogous derivations of hierarchical population inference in GW literature (Farr et al., 2015b; Gaebel et al., 2019; Mandel et al., 2019b).

3.2.1 Model definitions

For this paper, we model the luminosity evolution of KNe using a two-parameter, linear family of light curves (as adopted in Kasliwal et al. 2020). However, we will discuss extensions of our framework to other models as well. The absolute magnitude (M) in a

given filter λ is given as a linear function of time (t),

$$M^{\lambda}(t) = M_0 + \alpha\,(t - t_0) \tag{3.1}$$

where t_0 is the initial time of the KN transient. We can see that the two parameters (M_0, α), which represent an initial absolute magnitude and evolution rate respectively, completely define the evolution at all times. Therefore, for this simplistic parameterization, $\vec{\theta} = \{M_0, \alpha\}$. We emphasize that our motivation to implement such a simple model is to demonstrate the framework and due to the fact that we rely on follow-up observations of KNe up to 3 days following the merger time, where such models are a relatively good fit to the data (see Sec. 3.3.3 and Sec. 3.4).

Before we begin with our derivation, we will state our notation as follows:

- N_E : Total number of events that were followed up, indexed by i.
- N_F : Total number of fields-of-view for which EM observations have been recorded, indexed by f. For purposes of improved reference model subtraction, many optical/infrared surveys use discrete fields for observations rather than allowing complete freedom (Ghosh et al. 2017, Coughlin et al. 2018a and references therein). However, this can be generalized to any discretization of the sky such as HEALPIX (Hierarchical Equal Area isoLatitude Pixelization[2]; Górski et al. (2005)) if needed.
- N_f : Total number of observations for field f.
- t_j^f : Time of observation, indexed by j for each field f over the duration of follow-up of the event. j would run over the total number of observations for each field (N_f).

[2]https://healpix.sourceforge.io/

- t_0 : Initial time of the KN transient, which corresponds to the initial absolute magnitude M_0
- $\bar{f}$: Index for fields not including the field f.
- $\bar{F}$: Hypothesis that the KN is not in any of the observed fields.
- A : Hypothesis that the event is of astrophysical origin.
- T : Hypothesis that the event is of terrestrial origin (implying that the event is spurious).
- $P^i(A)$: The probability of the i^{th} event being of astrophysical (A) origin. This is an estimate provided by the LIGO-Virgo-KAGRA collaboration for the associated GW event. It can either be a low-latency estimate or an update provided after a refined analysis.
- $\{d^i\}$: The set of EM data associated with all events, indexed by i. We will further index this data by the field index f and time of observation index j, in our derivation below. For this study, we take our data to be the set of limiting (apparent) magnitudes $\{m_l^{i,f,j}\}$ in each field at the given time of observation.

3.2.2 Derivation of the model posterior

We begin our derivation of the model posterior with the basic equation of Bayes' law:

$$p(M_0, \alpha|\{d^i\}) = \frac{p(\{d^i\}|M_0, \alpha)p(M_0, \alpha)}{p(\{d^i\})} \tag{3.2}$$

where $p(\{d^i\}|M_0, \alpha)$ is the likelihood, $p(M_0, \alpha)$ is the prior distribution of the parameters M_0 and α, and $p(\{d^i\})$ is the evidence. We carry out analyses based on different prior

assumptions and show the effect it has on the posterior distribution of the KN parameters in Sec. 3.3. The likelihood represents the probability density of observing the data d^i given a model, for a set of events indexed by i, while the evidence is the probability of observing the data, marginalised over all parameters and serves as a normalization factor in the inference. Further, each event and its associated data are assumed to be independent. The likelihood $p(\{d^i\}|M_0, \alpha)$ can then be written as a product over events.

$$p(\{d^i\}|M_0, \alpha) = \prod_{i=1}^{N_E} \left[p(d^i|M_0, \alpha) \right] \tag{3.3}$$

There are two possibilities for any given event – either the event is astrophysical (A) or it is non-astrophysical/terrestrial (T). We note that the probability of the latter hypothesis is $(1 - P^i(A))$. We thus split the likelihood into two terms using the relative probabilities of each hypothesis,

$$\begin{aligned} p(\{d^i\}|M_0, \alpha) \quad = \quad & \prod_{i=1}^{N_E} \Big[p(d^i|M_0, \alpha, A) P^i(A) \\ & + p(d^i|T)(1 - P^i(A)) \Big]. \end{aligned} \tag{3.4}$$

The assumption in the last term in the parentheses is that the contribution to the likelihood cannot depend on the parameters of the KN model if the event is of terrestrial origin. This is straightforward to check because in the case of a purely terrestrial event ($P^i(A) = 0$), we must recover the prior when performing inference.

We now use the fact that, for any event (indexed by i), EM observations are distributed over N_F fields (indexed by f) at times of observation (indexed by j) such that every observation has associated limiting magnitudes ($m_l^{i,f,j}$). As stated above, we take our data d^i for each event to be the set of these observed limiting (apparent) magnitudes $\{m_l^{i,f,j}\}$,

i.e., $d^i \equiv \{m_l^{i,f,j}\}$. The likelihood thus becomes,

$$p(\{d^i\}|M_0,\alpha) = \prod_{i=1}^{N_E}\Big[p(\{m_l^{i,f,j}\}|M_0,\alpha,A)P^i(A) + p(\{m_l^{i,f,j}\}|T)(1-P^i(A))\Big]. \quad (3.5)$$

Furthermore, under the astrophysical hypothesis (A), the likelihood can be split into two more terms given that there are two possibilities for the KN event:

- The KN is located within an observed field f and consequently, not in any of the other fields ($\bar{f}$). In this case we need to find the probability that the KN is within a field f i.e., $P(f)$ and sum the contributions to the likelihood from each field. The overall likelihood contribution from this hypothesis is

$$\sum_{f=1}^{N_F}\Big(p(\{m_l^{i,f}\}|M_0,\alpha,A,f)P(f)\prod_{\substack{\bar{f}=1,\\ \bar{f}\neq f}}^{N_F}p(\{m_l^{i,\bar{f}}\}|A,f)\Big)$$

- The KN event is not located in any observed field (hypothesis $\bar{F}$). This case has a probability equal to $(1-\sum_{f=1}^{N_F}P(f))$. The overall likelihood contribution from this hypothesis is

$$\Big(1-\sum_{f=1}^{N_F}P(f)\Big)\prod_{f=1}^{N_F}p(\{m_l^{i,f}\}|A,\bar{F})$$

When information about a GW candidate event is released, it contains the 3D sky probability distribution of the location of the event, which includes the luminosity distance (d_L) to the source (Singer et al., 2016b,a). Using this, it is straightforward to compute

the probability for a KN to be present in a given field. Referring to Eq. 3 in Singer et al. (2016b), the sum of probabilities over the sky is

$$P(f) = \sum_{k=0}^{N_{pix}^{f}} \rho_k, \tag{3.6}$$

where the sum is over the N_{pix}^{f} pixels that are contained within field f and ρ_k is the probability of the event being in pixel k. The likelihood, written in terms of hypothesis contributions stated above, then becomes

$$\begin{aligned} p(\{d^i\}|M_0,\alpha) \;=\; & \prod_{i=1}^{N_E}\Bigg[\Bigg(\sum_{f=1}^{N_F}\Big(p(\{m_l^{i,f}\}|M_0,\alpha,A,f)P(f) \\ & \prod_{\substack{\bar{f}=1,\\ \bar{f}\neq f}}^{N_F} p(\{m_l^{i,\bar{f}}\}|A,f)\Big) \\ & +\Bigg(1-\sum_{f=1}^{N_F}P(f)\Bigg)\prod_{f=1}^{N_F}p(\{m_l^{i,f}\}|A,\bar{F})\Bigg)P^i(A) \\ & +(1\;-\;P^i(A))\prod_{f=1}^{N_F}p(\{m_l^{i,f}\}|T)\Bigg], \end{aligned} \tag{3.7}$$

where the second and third terms in the brackets correspond to the hypotheses that the KN position is outside all the observed fields and that the event is terrestrial in nature, respectively.

Since the observations in each field will have observation times associated with them, each field observation would constrain the model independently. Thus, the likelihood term for each field can be written as a product over the number of observations corresponding to that field.

$$
\begin{aligned}
p(\{d^i\}|M_0,\alpha) \;=\; & \prod_{i=1}^{N_E}\Bigg[\Bigg(\sum_{f=1}^{N_F}P(f)\Big(\prod_{j=1}^{N_f}p(m_l^{i,f,j}|M_0,\alpha,A,f)\prod_{\substack{\bar{f}=1,\\ \bar{f}\neq f}}^{N_F}\prod_{j'=1}^{N_{\bar{f}}}p(m_l^{i,\bar{f},j'}|A,f)\Big)\\
& +\Bigg(1-\sum_{f=1}^{N_F}P(f)\Bigg)\prod_{f=1}^{N_F}\prod_{j=1}^{N_f}p(m_l^{i,f,j}|A,\bar{F})\Bigg)P^i(A)\\
& +(1\;-\;P^i(A))\prod_{f=1}^{N_F}\prod_{j=1}^{N_f}p(m_l^{i,f,j}|T)\Bigg]
\end{aligned}
\tag{3.8}
$$

We now focus on the first term in the likelihood for each field $p(m_l^{i,f,j}|M_0,\alpha,A,f)$. In order to simplify this term and derive an expression for the same, we note that, in reality, a telescope measures an apparent magnitude (m_j) instead of an absolute magnitude. One can rewrite this likelihood term, using conditional probability, as an integral over the apparent magnitude of the KN event.

$$
\begin{aligned}
& p(m_l^{i,f,j}|M_0,\alpha,A,f) = \\
& \int_{-\infty}^{\infty} p(m_l^{i,f,j}|m_j)p(m_j|M_0,\alpha,A,f)dm_j
\end{aligned}
\tag{3.9}
$$

The relationship between the apparent magnitude (m), absolute magnitude (M) and luminosity distance (d_L) of an astrophysical source is given as

$$
m = M + 5\log_{10}\left(\frac{d_L}{10\text{pc}}\right) \tag{3.10}
$$

or equivalently,

$$d_L = 10^{\left(\frac{m-M}{5}\right)} \left(\frac{1}{10^5}\right) \mathrm{Mpc}. \tag{3.11}$$

The above formulae do not include the effects of extinction. We account for Milky Way extinction in our framework by appropriately modifying the limiting magnitudes for each field and filter. We make use of the `dustmaps` package (Green, 2018) and its implementation of the SFD dustmap (Schlafly & Finkbeiner, 2011) to derive extinction values. Also, from Eq. 3.11, we can derive a limiting distance $d_{lim}^{i,f,j}$ for a corresponding limiting magnitude $m_l^{i,f,j}$. The intrinsic parameters of the KN (M_0, α) along with the observation time (t_j) uniquely determine the absolute magnitude $(M_j(M_0, \alpha))$ of the KN, at any given time. Eq. 3.11 shows that for such a given absolute magnitude M, the apparent magnitude and distance are dependent variables that uniquely define each other. It is possible to relate the apparent magnitude distribution $(p(m_j|M_0, \alpha, A, f))$ in the integral above to the marginal distance distribution $(p_f(d_L))$ for each field f, which can be derived from the GW skymap, as

$$p(m_j|M_0, \alpha, A, f) = p_f(d_L) \frac{d\, d_L}{dm_j}(M_0, \alpha). \tag{3.12}$$

We can thus rewrite the integral in Equation 3.9 as

$$p(m_l^{i,f,j}|M_0, \alpha, A, f) = \int_0^\infty p(m_l^{i,f,j}|m_j(d_L, M_0, \alpha)) p_f(d_L) d\, d_L. \tag{3.13}$$

Since this is a non-detection study, the only viable limiting magnitudes for non-detection are those that are strictly shallower (brighter) than the apparent magnitude from the KN model. We implement this by using a uniform distribution function for the conditional density $p(m_l^{i,f,j}|m_j(d, M_0, \alpha))$ as,

$$p(m_l^{i,f,j}|m_j(d_L, M_0, \alpha)) = k \begin{cases} \frac{1}{(m_j - m_l^{i,f,j})} \; ; \; m_j \leq m_l^{\text{high}} \\ \frac{1}{(m_l^{\text{high}} - m_l^{\text{low}})} \; ; \; m_j > m_l^{\text{high}} \end{cases} \tag{3.14}$$

where m_l^{low}, m_l^{high} are the lower and upper limits of the range of limiting magnitudes from the survey or distance information, respectively and k is a normalization constant that will be discussed shortly. See Sec. 3.2.3 for a more detailed discussion on the choice of these limits. Further, it is important to account for the probabilistic nature of each limiting magnitude when considering the likelihood of any given model. We incorporate this requirement into our likelihood with a logistic function $\Phi(d_L - d_{lim}^{i,f,j})$. The logistic function ensures a smooth turnover in the likelihood between distances (apparent magnitudes) that pass the limiting distance (limiting magnitude) constraints and those that do not. From Equation 3.11, we can write the logistic function in terms of the distance as,

$$\Phi(d_L - d_{lim}^{i,f,j}) = \frac{1}{1 + e^{-a(d_L - d_{lim}^{i,f,j} + b)}}. \tag{3.15}$$

We choose the constants a and b in Equation 3.15 based on errors in the limiting magnitude such that a 3-σ error in $m_l^{i,f,j}$ corresponds to the distance at which the logistic function in Equation 3.15 is set to the cumulative probability weight of a Gaussian distribution beyond the lower 2-sigma limit ($\sim 2.3\%$). Combining Eqs. 3.14 and 3.15, the likelihood term in Eq. 3.13 can be evaluated up to a normalization constant k.

Since the total likelihood in Eq. 3.8 is a sum of probability densities, care must be taken to normalize each term, corresponding to each hypothesis, separately. The constant k can be derived by normalizing the likelihood term in Equation 3.13 between the appropriate limiting magnitude limits, or more directly between appropriate limiting distance limits:

$$k = \frac{1}{\int_{m_l^{\rm low}}^{m_l^{\rm high}} p(m_l^{i,f,j}|M_0, \alpha, A, f) dm_l^{i,f,j}}. \tag{3.16}$$

These limits can be chosen based on the extent of the marginal distance distribution for each field. We provide specific details of our assumptions for these limits in Sec. 3.3.

This normalization also ensures that we account for selection effects based on the limiting magnitude limits of the survey. We defer the discussion of the impact this has on the inference to Sec. 3.2.3. The remaining terms in the field (f), non-field ($\bar{f}$) and terrestrial (T) hypotheses from Equation 3.8 must be normalized. We assume that each of these terms follows a uniform distribution between the survey limits $m_l^{\rm low}$ – $m_l^{\rm high}$. This assumption largely simplifies the form of the likelihood. While it is not necessary to assume such a form for each of these terms, and one can construct more complex distributions based on realistic data, this choice does not impact the inference because these distributions must necessarily be independent of the model parameters. This gives us a normalized density of

$$\begin{aligned} p(m_l^{i,\bar{f},j'}|A, f) &= p(m_l^{i,f,j}|A, \bar{F}) = p(m_l^{i,f,j}|T) \\ &= \frac{1}{\left(m_l^{\rm high} - m_l^{\rm low}\right)} \end{aligned} \tag{3.17}$$

This simplifies the likelihood in Equation 3.8 to give us a posterior

$$p(M_0, \alpha|\{d^i\}) \propto \prod_{i=1}^{N_E} \left[\left(\sum_{f=1}^{N_F} \left(\frac{\prod_j p(m_l^{i,f,j}|M_0, \alpha, A, f)}{\prod_j p(m_l^{i,f,j}|A, \bar{f})} \right) P(f) \right) \right.$$

$$+\left(1-\sum_{f=1}^{N_F} P(f)\right)\Bigg) P^i(A)$$
$$+\left(1 - P^i(A)\right)\Bigg] p(M_0,\alpha). \tag{3.18}$$

3.2.3 Impact of using survey limits and distance limits on inference

We derived our model posterior for the framework in Sec. 3.2.2. As seen in Equation 3.16, an important quantity to compute for the posterior is the normalization factor k which depends on the choice of upper limits $m_l^{\rm low}$, $m_l^{\rm high}$ and model parameters (M_0, α). Such a factor is akin to accounting for selection effects (see Mandel et al. 2019b) where one has to normalize the likelihood of observing a given model (M_0, α) by the range of data supported by the model. From Eq. 3.11, it is possible to express upper limits for a model equivalently in terms of the apparent magnitude or the distance. Thus, a range in one of the quantities directly specifies a range in the other. The choice of which quantity to use to calculate, $m_l^{\rm low}$ and $m_l^{\rm high}$, significantly affects the result of the inference. There are two ways to select specific values for these normalizing parameters:

- Survey Limits: A straight-forward method is to choose $m_l^{\rm low}$ and $m_l^{\rm high}$ directly from survey data when the telescope is observing. From Equation 3.11, this directly impacts the range of distances permitted for a given model (M_0, α) and gives a different normalization value for each model. Such a method ensures that the normalization realistically accounts for model biases in the case of non-detection.

- Distance Limits: Alternatively, we can choose to use the distance posterior from the GW skymap data as our source of ground truth such that we calculate $m_l^{\rm low}$ and $m_l^{\rm high}$ based on the full range of possible distances[3]. This will change the values of

[3]Computationally, we bound the distance between a realistic lower limit and the upper 5-σ value from the distance posterior.

$m_l^{\rm low}$ and $m_l^{\rm high}$ for each model. However, as the range in distance is the same for each model this ensures that the normalization factor is the same.

We note that our preferred results in this paper are those that use realistic survey upper limits. Unless stated otherwise, our reference to results in general will be with this choice. We present the differences that result from these two choices in Sec. 3.3.1.

3.3 KILONOVA INFERENCE USING GW190425

GW190425 was a highly significant ($p_{\rm astro} \sim 0.999$; Abbott et al. 2020a) GW event that was followed up by ZTF (Coughlin et al., 2019d) with an overall sky coverage of $\sim 32\%$ of the total skymap. Inferences on the component masses of the detected binary show it to be consistent with a BNS, although the possibility of either or both components being BHs cannot be ruled out from GW data alone. Here, we present results using the Bayesian framework `nimbus` described here with upper limits from the ZTF follow-up of GW190425 to derive posterior constraints on KN parameters of the model light curve for BNS mergers. We note that unlike the band-specific linear evolution shown in Eq. 3.1 we adopt a single "average-band" linear model with parameters (M_0, α) for our analyses presented here. This "average-band" model effectively assumes the same color evolution in all bands, allowing us to use ZTF observations in all filters for our analysis. This simplified model is conducive for testing the `nimbus` framework as it significantly reduces the model parameter-space (since kilonova models predict a wide diversity in expected color evolution). For example, using this linear model fit, GW170817 has $M_0 = -16.6$ mag and $\alpha = 1$ mag day^{-1} (Kasliwal et al., 2020). Our analyses rely on two different prior distribution choices for (M_0, α) – (i) uniform or agnostic priors (explained in Sec. 3.3.1) and (ii) astrophysical priors motivated from theory and numerical modeling (explained in Sec. 3.3.3). We limit our analyses to use follow-up data up to 3 days from the trig-

ger time since realistic models predict that most kilonovae will fade beyond the median ZTF limiting magnitude of 21 m_{AB} (for this event) within 72 hours after trigger time (see Sec. 3.4).

In order to limit the effects of Milky Way extinction in the fields surveyed, we place a conservative threshold by excluding fields which have $E(B-V) > 2$ mag. For the remainder of the paper, we make a simplifying assumption that the KN associated with GW190425 is located within the searched region.[4] We ran simulations taking the full GW190425 skymap into account and found the results to be largely unconstraining; hence we adopt the above assumption in order to demonstrate the constraints possible with `nimbus` in an ideal sky coverage scenario. Our constraints on KN model parameters, obtained using both prior choices stated above, are displayed in Table 3.1. In order to derive our constraints and plot our posterior probabilities in this paper, we make use of an interpolating or smoothing function such as the Gaussian Process module from `scikit-learn` (Pedregosa et al., 2011) to interpolate between our original samples from priors. We have checked that uncertainties from these interpolations (see Fig. 3.2) are within the statistical variations of the observed limiting magnitudes across the ZTF quadrants for each field of observation, where these variations are $\geq$ **0.1 mag** for a majority of fields. Sec. 3.3.1 with uniform priors demonstrates the functionality of the framework. In particular, our results in this Section show the posterior constraints that are possible using the framework. In addition, we show how a general inference is sensitive to variations in sky coverage and $p_{\rm astro}$. We also use this Section to illustrate the differences in results based on the two different normalization choices as explained in Sec. 3.2.3: choosing the faint and bright apparent magnitude limits based on the observed range from ZTF (Survey Limits) *or* based on the minimum and maximum distances from the GW distance

[4] `nimbus` has the capability to accommodate for the excluded part of the skymap (see Fig. 3.2).

posterior (Distance Limits). Sec. 3.3.3 demonstrates the ability to test astrophysical priors within the `nimbus` framework.

3.3.1 Uniform priors

We first implement the framework assuming uniform priors for our model parameters $M_0 \sim \mathcal{U}(-20, -10)\,\mathrm{mag}, \alpha \sim \mathcal{U}(-1, 2)\,\mathrm{mag\,day}^{-1}$. According to our convention (see Eq.3.1) a negative evolution rate would imply a rising light-curve for the kilonova while a positive one would be decaying. While $\alpha < 0$ appears implausible based on our BNS KN model fits (see Sec. 3.3.3), KNe from NSBH systems can exhibit a slow rise (Anand et al., 2020) that could take $\gtrsim$2 days to peak. Within our time window of observations of 3 days, a NSBH KN model may be better approximated by a rising linear model than a fading one. Thus, we adopt a broad range for our evolution rate prior to accommodate rising to rapidly decaying KN models. Our prior on the initial magnitude is similarly broad, spanning a large fraction of the known transient phase-space (Kasliwal, 2011). Such a prior is uninformative with respect to the realistic emission models of KNe that have implications for how (M_0, α) could be distributed. The posterior densities we obtain via the framework are shown in the left panel of Fig. 3.1. Broadly, we see that, as expected for a non-detection, there is more posterior support for dimmer models (larger values of M_0 and α) than brighter ones (smaller values of M_0 and α). Another expected trend is the increase of support for brighter M_0 values with respect to the evolution rate as we vary α from ~ -1 to $1\,\mathrm{mag\,day}^{-1}$. A significant part of the parameter space that belongs to bright and rising models ($M_0 \lesssim -18$ and $\alpha \lesssim 0$) is disfavored over the rest of the models by factors of $\sim 10 - 100$. For most of the parameter space, where $M_0 \gtrsim -15$, our results cannot place any constraints.

The right panel of Fig. 3.1 also compares the posterior constraints we obtain with

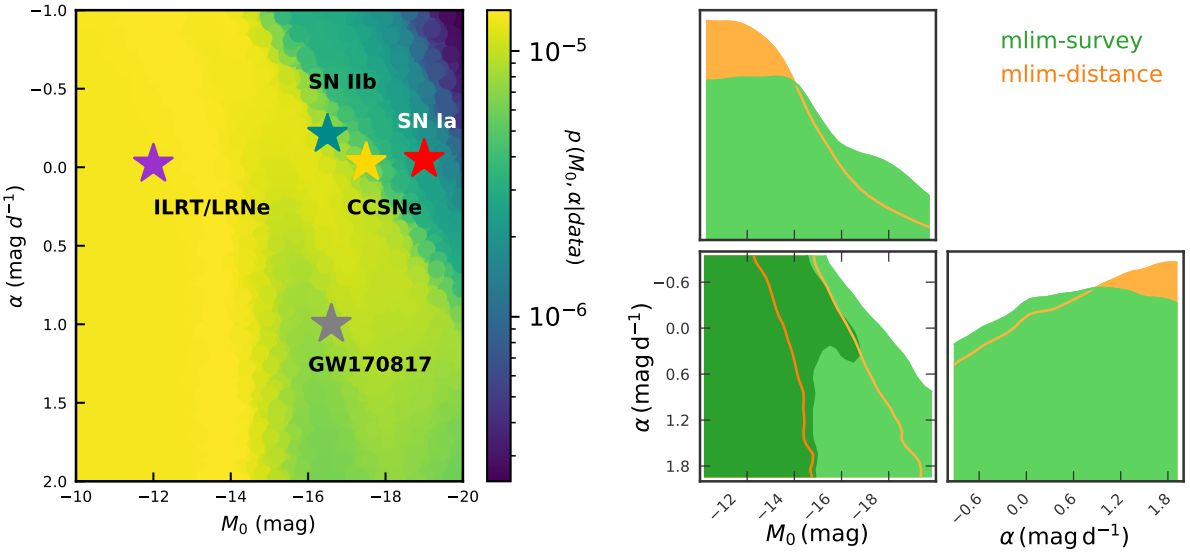

Figure 3.1: (left) 2-D posterior probability plot of KN model parameters (initial absolute magnitude M_0, evolution rate α) with uniform priors, $M_0 \sim \mathcal{U}(-20, -10)\,\mathrm{mag}, \alpha \sim \mathcal{U}(-1, 2)\,\mathrm{mag\,day}^{-1}$, and normalization over realistic Survey Limits. Representative points are shown for the characteristic peak magnitude and rise rate (derived from the characteristic timescale) for some categories of transients (Kasliwal (2011), Fremling et al. in prep) – SN Ia (red), Core Collapse SNe-CCSNe (gold), Faint, fast SNIIb (dark-cyan), ILRT/LRNe (dark-orchid) and GW170817 (grey).(right) Corner plot showing the 2-D and corresponding 1-D marginalized posterior distributions of the KN model parameters for the two different normalization schemes detailed in Sec. 3.2.3 — using realistic Survey Limits from ZTF data for GW190425 which are between 15–23 mag (green; `mlim-survey`) and Distance Limits obtained for each model draw using 5σ distance limits obtained from the skymap distance posterior for each field (orange; `mlim-distance`). Contours indicate 68% and 95% confidence regions. Non-monotonic features in both panels (eg: 68% green contour in the right panel) indicate the effects of model normalization. Details in Secs. 3.2.3,3.3.1.

two different normalization choices as explained in Sec. 3.2.3. The inference derived using realistic survey limits (`mlim-survey`; green contours) rely on the range of limiting magnitudes obtained from ZTF during the follow-up of GW190425. For this event this corresponds to range limits of ($m_{\rm low} \approx 15, m_{\rm high} \approx 23$). On the other hand posteriors obtained using distance limits (`mlim-distance`; orange contours) rely on the entire range of posterior distances from the 3-D skymap for the event. While constraints from the two choices are quite similar with respect to the evolution rate, the `mlim-survey` method provides more support to models on the brighter end of the M_0 distribution compared to the `mlim-distance` method. This is understandable since having a restricted range of limiting magnitudes from the survey reduces the range of viable distances for brighter models thereby providing a smaller parameter space that satisfies the likelihood. Accounting for this fact in the likelihood as a selection effect leads to an upweighting of these brighter models with respect to the `mlim-distance` method. This is also the reason we see non-monotonic features in the 2-D posterior distributions with the `mlim-survey` method in both panels of Fig. 3.1. The effects of normalization arise the most for models that are at the marginal boundary with respect to the upper limits. As mentioned previously, our preferred results in this paper are those that use the `mlim-survey` method.

As seen from Table 3.1, the 90% upper limit with a uniform prior is about $M_0^{90\%} = -16.63$ mag. We compare the result derived here to the probability of zero detections as a function of absolute magnitude shown in Fig. 9 of Kasliwal et al. (2020), which indicates a $\sim 7\%$ probability for models with a similar initial absolute magnitude. Although the two separate constraints are consistent, there are significant differences between the two formalisms overall. The first is that our analysis assumes that an associated KN fell within the observed region. If we relax this assumption and use the ∼32% sky coverage in total

for this event by ZTF, our inference over the entire skymap region does not yield any meaningful constraints, as expected.

The second difference is that in this work, we infer the properties of a KN associated with GW190425, while the main result of Kasliwal et al. (2020) places constraints on the luminosity function of the KN population as a whole. While strong constraints on the KN emission from a *single* GW event are possible with a combination of complete sky coverage and deep upper limits, analyzing KN population properties importantly relies on *several* events observed with decent sky coverage and depth. We note, however, that GW190425 likely contributes significantly to the constraints in Kasliwal et al. (2020) given its nearby distance and ZTF median depth ($m \approx 21$ mag).

The 90% limit stated above is also significant in that it represents the extrapolated peak magnitude of GW170817 with a average decay rate of $1\,\mathrm{mag\,d^{-1}}$ (Kasliwal et al., 2020). From the left panel in Fig. 3.1, we can see that the data for the non-detection of a kilonova associated with GW190425 are still consistent with these parameters.

Fig. 3.2 demonstrates how variations in sky coverage and p_{astro} can impact inferences in such a study in general. Our assumptions and derived constraints in this work correspond to ($p_{\mathrm{astro}} \sim 0.999$, sky coverage $= 100\%$). However, as the sky coverage or astrophysical probability drops, the contribution of the survey upper limits to the posterior weakens and the constraints become more broad. In particular, below a certain value for these parameters, the median apparent magnitudes inferred for the KN are brighter than the median ZTF upper limits, pointing to the fact that at these values the alternative hypotheses - of either the KN being in a part of the sky where we do not have any observations or the KN event being a Terrestrial event - have more probability support. This result also demonstrates the functionality of the framework to account for arbitrary values of these probabilistic factors that impact inference.

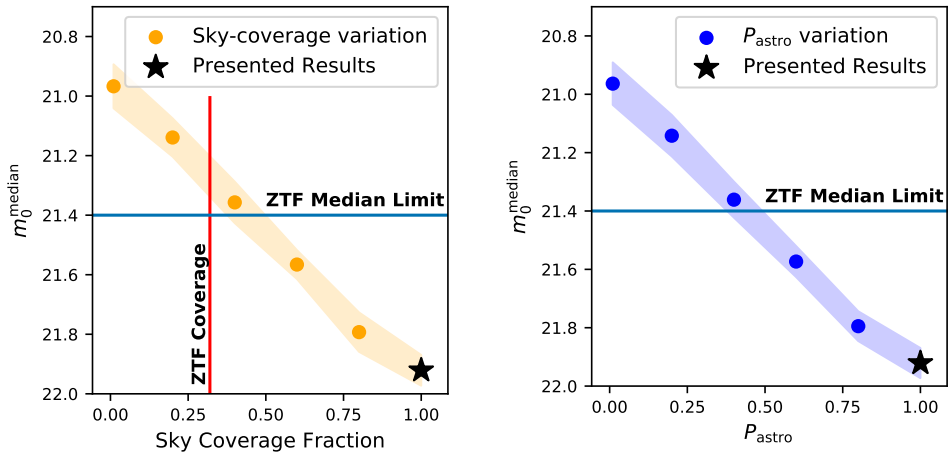

Figure 3.2: Variation in the median of the initial apparent magnitude distribution (assuming the source is at the mean luminosity distance from the 3-D skymap) as a function of sky-coverage (left) and probability of astrophysical origin P_{astro}(right). As the sky-coverage/P_{astro} decreases (increases), constraints on the population parameter become weaker (stronger). Colored bands in both plots indicate $2-\sigma$ error regions from the interpolation of posterior probabilities as mentioned in Sec.3.3. Horizontal lines at $m = 21.4$ mag in both plots indicate the median limiting magnitude across the 3 day ZTF observations for GW190425. Red vertical line in left plot indicates the actual sky coverage by ZTF.

3.3.2 Comparison with `simsurvey`

In order to benchmark our results against those from complementary methods in the literature, we compare the limits we obtain via `nimbus` with those from the open-source simulator software `simsurvey`[5] (Feindt et al., 2019). `simsurvey` simulates KN detections (or injections) based on survey limits for any given event (Sagués Carracedo et al., 2021). We estimate the efficiency (or probability) of detecting a KN of a given initial absolute magnitude and linear evolution rate by comparing detections with the total injections within the observed fields. The software takes as input the ZTF pointings and information (i.e., the observation time, limiting magnitude, filters, right ascension and declination

[5] https://github.com/ZwickyTransientFacility/simsurvey

for each field and CCD) for the first three days after the merger, and the 3D GW skymap for any given GW event. We simulate 100,000 KNe for a given absolute magnitude and evolution rate throughout the 3D GW probability region (see Fig. 3.3). We assume a linear, colorless lightcurve model as stated in Sec. 3.2.1. Our detection criteria requires the KN to be detected at least once by ZTF: given actual detection experiments this is a necessary but likely insufficient criterion for identification, since both color information and evolution rate are needed to separate KNe from false positives (Andreoni et al., 2020). For example, the gamma-ray burst afterglows that have been discovered in the past with the ZTF Realtime Search and Triggering (ZTFReST; Andreoni et al. 2021a) pipeline have exhibited rapid evolution and reddening, requiring detections in both g- and r-bands, with $\geq$2 detections in either band for solid identification. Using `simsurvey` we account for Milky Way extinction and exclude any KNe with $E(B-V) > 2$ mag. This process is repeated for a range of magnitudes (100 bins between -10 and -20 mag) and evolution rates (31 bins from -1 and 2 mags per day) resulting in a grid of efficiencies. This grid of efficiencies are then converted into non-detection probabilities (see Fig. 3.3).

As this is a non-detection study, `nimbus` generates posterior probabilities for models that are consistent with non-detection using observational upper limits; we compare the posterior support for models from `nimbus` with the detection efficiency estimates for the same models from `simsurvey`. We normalize the non-detection probabilities in the `simsurvey` model grid to sum to 1 in order to compare against `nimbus` . In Fig. 3.4, we show the 2-D and 1-D marginalized posterior distributions for the two light curve parameters from these formalisms.

We note that for `simsurvey`, the non-detection probability is calculated as $1.0 - \epsilon_i$, where ϵ_i is the recovery efficiency for a KN with a given absolute magnitude and evolution rate. Therefore, it naturally follows that as the initial absolute magnitude gets dim-

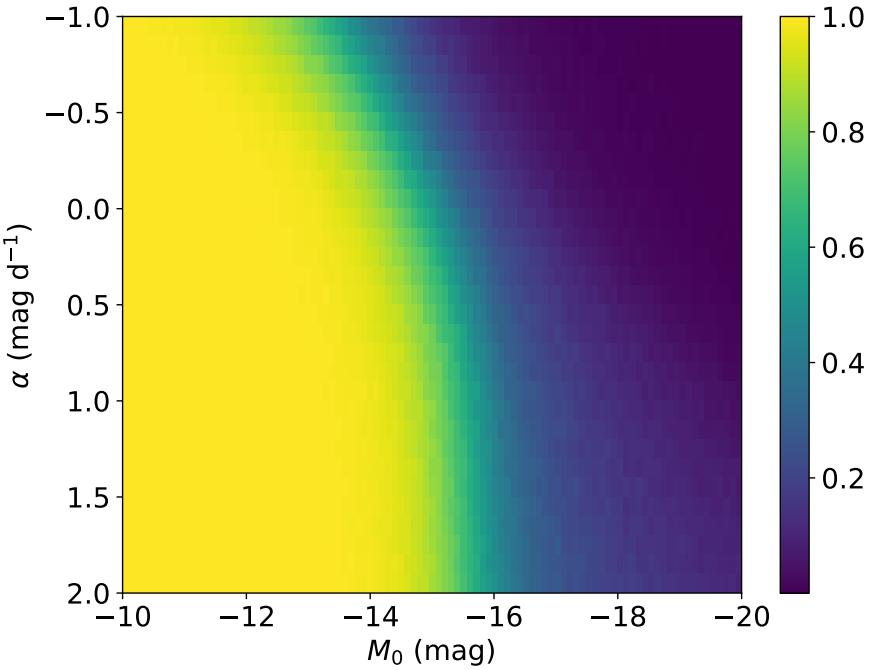

Figure 3.3: Non-detection probability 1-ϵ_i, where ϵ_i is the recovery efficiency (number recovered / number injected) at a given absolute magnitude and evolution rate, for the grid of KNe simulated and recovered using `simsurvey`. We simulate 100,000 KNe in each bin, with magnitudes ranging from -10.0 to -20.0 mag and evolution rates ranging from -1.0 to 2.0 mag day^{-1}.

mer, our constraints get progressively worse. Likewise, going from rising to fast-fading KN models, the constraints become weaker.

In general, these comparisons illustrate consistency between the constraints inferred by the two methods on the brighter edge of the initial magnitude distribution, as evidenced by the 2-D posterior in Fig. 3.4. We observe a large overlap in the 1-D marginalized posteriors for evolution rate for both formalisms. In both our hierarchical Bayesian formalism and the frequentist simulation-based approach, we observe that as the model evolution rate changes from -1.0 mag day^{-1} to ~ 1.0 mag day^{-1}, constraints on KN models get progressively weaker. A rising KN is disfavored for values of M_0 on the brighter

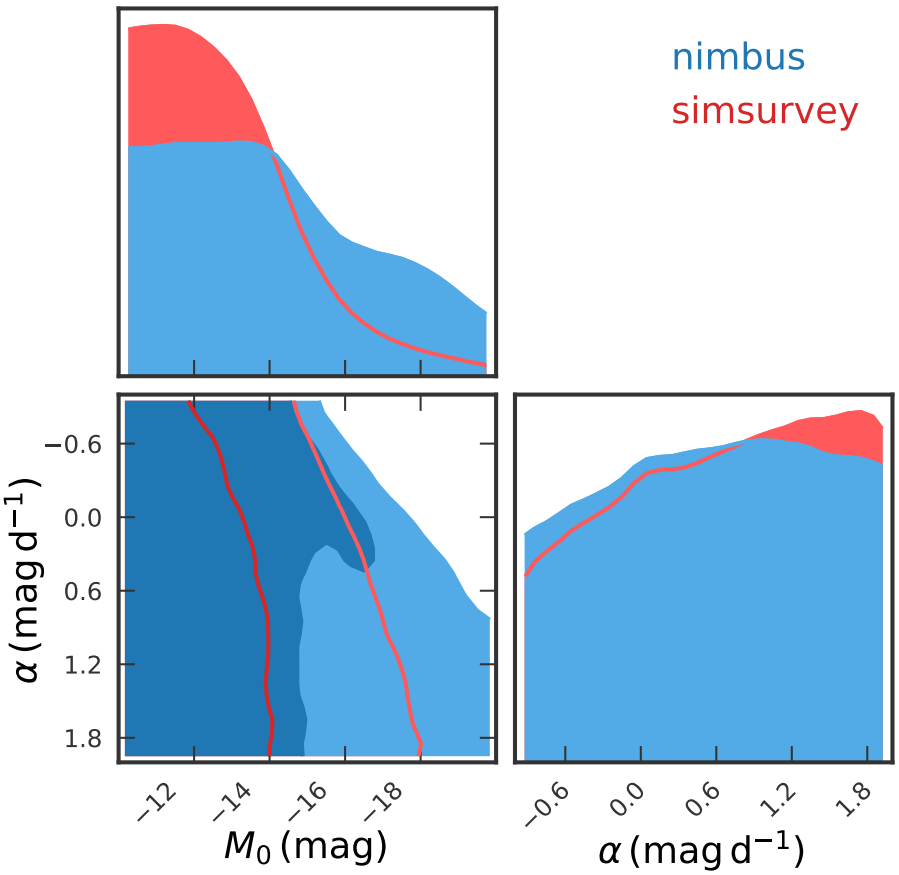

Figure 3.4: Comparison between `nimbus` and `simsurvey` with uniform priors. The corner plots compare the 2-D and corresponding 1-D marginalized posterior distributions for `nimbus` (blue) against the normalized non-detection probabilities from `simsurvey` (red). The 68% and 95% contours indicated on the plot demonstrate consistency between the two formalisms. We assume the same uniform priors in magnitude and evolution rate as for Fig. 3.1.

end of the initial magnitude range, as the transient would be brighter than these survey magnitudes. However, for evolution rates >1 mag day^{-1}, the effects of normalization in `nimbus` (see Sec. 3.2.3) take into account that the survey limiting magnitudes lend more support to faster-decaying models, while the nightly limits themselves place nearly

no constraints in this region of parameter space, leading to conservative estimates in the posterior curve relative to `simsurvey`. The 1-D magnitude posteriors reveal that `nimbus` has broader support for KN models of varying absolute magnitudes (plateauing around $M \gtrsim -15$) and more conservative constraints compared to `simsurvey` for the brightest initial magnitudes.

Fundamentally, these two approaches are different but complementary. The `simsurvey` analysis yields the probability of not detecting a KN with (M_0, α) given the observations. `nimbus` gives the posterior probability for a KN with (M_0, α) that *survives* the upper limits. Thus comparisons between these two approaches discussed here are analogous, but not exact. Note that while the results from `simsurvey` here might seem similar to those obtained in Fig. 3.1 using the `mlim-distance` method of normalization, we emphasize that our preferred results using the `mlim-survey` method are more realistic in that they use the actual observed range of ZTF limiting magnitudes from the follow-up of GW190425. As stated before, the `mlim-distance` method uses the entire range of viable distances from the 3D GW skymap. One reason the `simsurvey` results could be similar to this method is that the `simsurvey` method also performs simulations in the entire region of the skymap based on the GW distance posterior. In order to better understand our results from the two formalisms, we also compared model probabilities using data from a single field of observation. Our results in this case show greater agreement indicating that the differences in the main results arise from the fundamentally different treatment of combining multiple fields with varying upper limits, luminosity distance distributions and different methods of model normalization.

3.3.3 Astrophysical Priors

Variations in the masses, velocities, composition of the ejecta and inclination angle of the binary system result in different observed KN morphologies. BNS mass ejection mechanisms are categorized into two broad classes: dynamical ejecta and post-merger or wind ejecta (Nakar, 2019). The tidal mass ejection occurring within $\sim$10 ms of the final inspiral stage is referred to as the dynamical ejecta. Bound NS material, which forms an accretion disk around the merger remnant, releases an outflow termed as the wind ejecta due to magnetically-driven, disk and neutrino winds.

Using priors inspired from realistic astrophysical models of KNe based on simulations, we present our Bayesian constraints with GW190425 in Fig. 3.5. These priors are derived from surrogate models (Coughlin et al., 2018b) trained on the outputs of the Monte Carlo Radiative-transfer code POSSIS (Bulla, 2019). Previous studies have underscored the importance of using astrophysical lightcurve priors in interpreting the emission from GW190425 (Barbieri et al., 2021; Foley et al., 2020; Kyutoku et al., 2020; Dudi et al., 2021; Nicholl et al., 2021; Raaijmakers et al., 2021). Broadly speaking, the surrogate models, otherwise referred to as phenomenological models, use a machine learning technique to interpolate between data points. In this paper, we use a suite of 2D KN models assuming a three-component ejecta geometry, with dynamical ejecta split between equatorial lanthanide-rich and a polar lanthanide-poor components, and a spherical disk-wind ejecta component at lower velocities and with compositions intermediate to lanthanide-rich and lanthanide-poor (Dietrich et al., 2020). The simulations cover four parameters: the inclination or the observer viewing angle ($\theta_{\rm obs}$), dynamical ejecta mass ($M_{\rm dyn}$), post-merger or wind ejecta mass ($M_{\rm wind}$), and half-opening angle for the lanthanide-rich dynamical ejecta component (ϕ).

We assume a $\phi = 30^{\circ}$ half opening angle and vary the other three parameters. Using

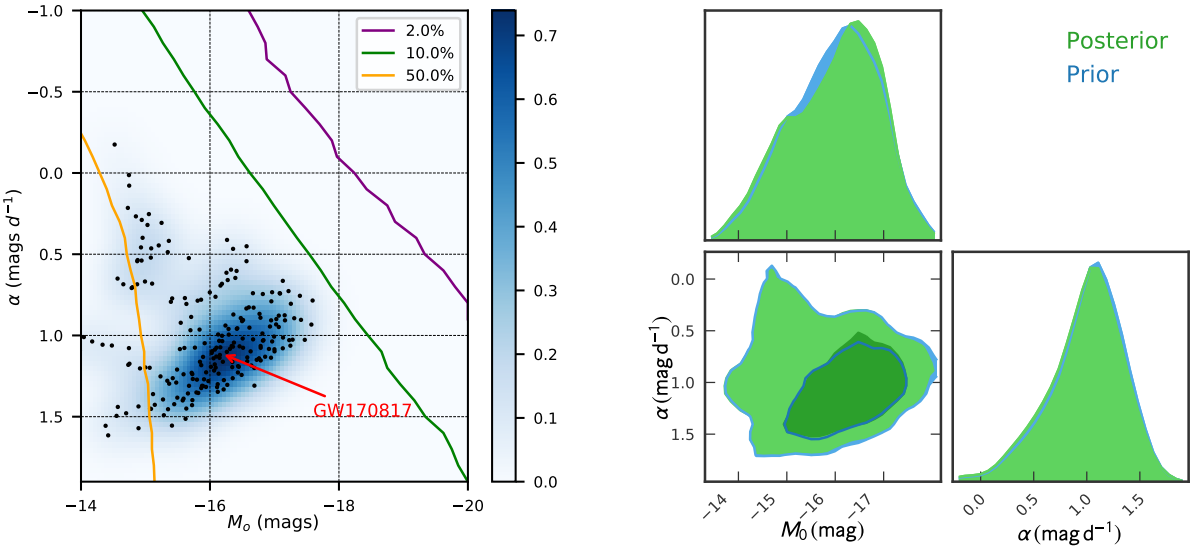

Figure 3.5: (left) Bolometric priors, informed by radiative-transport based KNe models (Bulla, 2019; Dietrich et al., 2020), showing regions of parameter space where particular luminosities and evolution rates are most probable or improbable for BNS KNe. To guide the eye, the best fit model for GW170817 is highlighted. The non-detection percentiles (solid lines) are calculated using `simsurvey`, as discussed in Sec. 3.3.3. (right) Corner plot showing the 2-D and corresponding 1-D marginalized posterior distributions (green) using model based priors (blue).Contours indicate 68% and 95% confidence regions.

the surrogate models, we predict BNS KN light curves for 10 viewing angles from a polar ($\theta_{\rm obs} = 0°$) to an equatorial ($\theta_{\rm obs} = 90°$) orientation, equally spaced in $\cos(\theta)$, and for the following ejecta masses: $M_{\rm dyn} \in [0.001, 0.005, 0.01, 0.02]$ and $M_{\rm wind} \in [0.01, 0.11]$ in steps of 0.02 $M_\odot$. In total, there are 240 BNS KN models. We then map from KN source properties (e.g., ejecta mass and inclination angle) to observables (peak magnitude and evolution rate) by performing lightcurve fits.

A typical simulated BNS KN rapidly rises to a maximum within a day or two and gradually decays. Since the decaying period dominates, we fit a linear model from the entire grid's median phase of the peak magnitude up to three days since the merger for

g-, r- and i-band KN lightcurves. We omitted 20 models that had a mean squared error greater than 0.1 from this process. These omitted models specifically had low $M_{\rm dyn}$ but high $M_{\rm wind}$. For each combination of source parameters, we then combine g-, r- and i-band peak magnitudes and evolution rates based on the number of simulated KNe in `simsurvey` that fall in the ZTF observed region of any specific filter. For GW190425, we have about 2614, 2930, and 168 out of 100,000 simulated KNe that fall in the region observed with g-, r- and i-band ZTF filters respectively. Gathering the grid-based values for peak absolute magnitudes and decay rates of KNe, we use kernel density estimation to construct a smooth probability density function and approximate the true distribution for the models considered. The left panel of Fig. 3.5 shows this grid-based prior model overlaid with `simsurvey` non-detection probabilities.

Effectively, the astrophysical prior reduces a large portion of the parameter space previously considered by the uniform prior choice. The 2%, 10%, and 50% non-detection percentiles estimated using `simsurvey` are plotted over the astrophysical priors. Though the probable prior region is mostly encompassed by the 50% curve, it lies entirely to the left of the 2% and 10% curves, indicating that our GW190425 ZTF observations are not deep enough to place stringent constraints over the astrophysical priors. This is reflected in the inference results from `nimbus` (right panel of Fig. 3.5) based on the astrophysical prior assumptions. Specifically, the posterior and prior contour lines overlap considerably, showing that almost all of the KN models supported by the astrophysical prior survive the upper limits. In general, this implementation demonstrates the ability to use theory and simulation-based astrophysical models within the `nimbus` framework and constrain them.

Prior Choice	$M_0^{90\%}$
Uniform-mlim	-16.63
Uniform-distance	-15.01
Astrophysical	-17.08

Table 3.1: 90% upper limit of the kilonova initial absolute magnitude (M_0) for the different prior choices in Sec.3.3

3.4 DISCUSSION AND FUTURE OUTLOOK

In this paper, we have presented a hierarchical Bayesian framework `nimbus` that leverages data from non-detections of probable KNe. This Python package utilizes GW and EM follow-up information from each candidate event to provide posterior distributions for KN model parameters. The framework also accounts for the probability of an event being astrophysical. Although the analysis presented here focuses on a single BNS event, GW190425, the framework has the capability to include multiple events. It is also straightforward to extend the framework to model the inference based on sub-populations of KN candidates such as BNS and NSBH mergers. We hope the multi-messenger astrophysics community finds use for and benefits from this package.

A current limitation of this study is that the framework does not account for events that have been detected in EM follow-up. In order to place stringent constraints on KN parameters, it would be ideal to include potential candidates for which there exists data from detected light curves. However, including information from detected events into the framework would involve non-trivial changes to the model likelihood and would necessitate an accurate understanding of survey selection effects. So far, GW170817 (Abbott et al., 2017b) is the only GW event to have been associated with a KN counterpart (Abbott et al., 2017c). Numerous studies in the literature (e.g., Cowperthwaite et al., 2017; Drout et al., 2017; Arcavi, 2018; Andreoni et al., 2020) have extrapolated follow-up data to arrive at an estimate of its initial absolute magnitude and decay rate. In particular, Kasliwal

et al. 2020 compared their results to an extrapolated initial magnitude of -16.6 mag with a decay rate of 1 mag per day. Our results do indicate non-negligible posterior support for such a model. Nevertheless, this represents a single point in model parameter space and we would instead require a number of detected events to inform the population of KNe. Further, restricting the study to non-detections is motivated by the fact that O3 did not yield any obvious EM counterparts. We defer the development of including detected events to a future study.

We presented results of our inference on GW190425 using two different prior choices for our model parameters (see Figs. 3.1 and 3.5). Our first choice, which is uniform in the parameters, is representative of an inference that is carried out with uninformative assumptions. Our second prior choice is based on surrogate models from Monte-Carlo radiative transfer simulations of KNe (Coughlin et al., 2018b; Bulla, 2019) and takes into account the effect of variations in ejecta masses and inclination angle on the resulting KN morphology. The inference using such a prior represents the possibility of testing realistic, physical models of KNe against upper limits obtained from surveys. While our implementation with uniform priors constrained the prior parameter space to a considerable extent and shows consistency with previous efforts (Kasliwal et al., 2020), the posterior results based on surrogate KNe models are largely uninformative with respect to the prior. Overall, these results show how priors on model parameters can influence the constraints obtained and the need to examine results in light of the prior distribution.

One of the assumptions we have made in presenting our results above is that the KN counterpart to GW190425 is localized within the surveyed region of the skymap. GW190425, as mentioned previously in Sec. 3.3, had an overall sky coverage by ZTF of $\sim 32\%$. Given that a significant fraction of the skymap is not surveyed and therefore would result in uninformative constraints, we made this assumption to demonstrate the

utility of the Bayesian framework. In LIGO-Virgo-KAGRA's fourth observing run, we expect that for ∼8-10% of BNS and NSBH systems discovered, ZTF will be able to observe >90% of the localization (Petrov et al., 2021), and hence our above assumption would hold reasonably true in those particular cases.

Furthermore, throughout this study we have assumed a kilonova luminosity evolution model that is linear in time. A linear model only needs two parameters to define it and our goal in this paper has been to demonstrate framework functionality at the cost of model accuracy. Such a simplistic choice might not be representative of realistic evolution models (see Metzger 2019) that depend on more complex parameters related to the binary system. In principle, it should be feasible to include arbitrary models for luminosity evolution since the framework only expects a function that returns predictions for the absolute magnitude of the KN as a function of time. For all priors applied, we consider only the first three days of evolution of the KN (and therefore the first three days of observations after the merger time of GW190425). This choice is motivated by the fact that ZTF is unlikely to detect a KN at the distance of GW190425 in the g- and r-bands after three days post-merger. More specifically, at four days, all KN models in our set have an apparent magnitude in the g- and r-bands fainter than the median depth of ZTF in this study (~ 21 mag).

In this work we also neglected color evolution in our studies of kilonova non-detections. In addition to differentiating observations in different filters, in the future we intend to account for the K-correction effect on kilonova color evolution which is especially relevant for cosmological sources. We will implement this feature in `nimbus` following the existing implementation in `simsurvey`.

We highlight here that due to the adaptability of `nimbus` to various lightcurve models and a hierarchical framework, it could even be used to jointly constrain the properties of

a potential kilonova and short GRB optical afterglow associated with the GW event (as in Dietrich et al. 2020, Pang et al. in prep) based on the rapid optical follow-up performed by various facilities.

In order to establish consistency with existing results in the literature, we compared our results to those from the simulator software `simsurvey`. As shown in Fig. 3.4, the two formalisms are largely consistent although some qualitative differences exist. In the future, with observations and upper limits from more events, it will be possible to test for further consistency between frameworks investigating KN populations.

In our specific implementation with astrophysical priors in Sec. 3.3.1, we used a prior on the KN luminosity parameters, i.e. the initial absolute magnitude and evolution rate that depends on intrinsic parameters such as the dynamical or wind ejecta masses. Our Bayesian approach makes it straightforward to convert our posteriors on the luminosity parameters into constraints on these intrinsic parameters. Alternatively, since the framework is agnostic to the KN model used, it should be possible to directly use priors on the physical parameters that govern the light-curve morphology. In such a case, the inference would directly constrain parameters such as the ejecta mass from the binary merger, although the computational feasibility of such an implementation needs to be investigated. The use of these astrophysical priors is based on including variations in the observer viewing (inclination) angle and its effect on each KN model. Non-trivial couplings between the observer angle and the signal-to-noise ratio of the GW signal can lead to some selection bias. To mitigate this effect in the future, we will select skymaps from a realistic distribution of GW signals detected by Advanced LIGO - Virgo (Petrov et al., 2021) which will inform the distribution of observer angles for our kilonova models.

Looking forward to O4 and beyond, we expect that `nimbus` will be an important framework for analyzing joint EM-GW observations. Petrov et al. 2021 predict a median

of $\sim$35 BNS yr^{-1} with O4 sensitivity and roughly double the number during O5. Thus, with several tens of EM follow-ups of BNS events from O4 and O5, we will use `nimbus` to place stringent population-level luminosity function constraints based on non-detections. For the well-localized ($\lesssim 100\,\mathrm{deg}^2$) and nearby ($\lesssim 200\,\mathrm{Mpc}$) events (predicted to range from 0-13 BNS mergers; Petrov et al. 2021) detected by Advanced LIGO - Virgo in O4 for which we have excellent optical sky coverage, `nimbus` is ideally placed to constrain the intrinsic kilonova properties which can translate to constraints on binary system parameters such as mass ratio and NS radius in the face of non-detection. A similar analysis of NSBH mergers is also feasible, though ejecta mass yield sensitively depends on the mass ratio of the system (e.g. Krüger & Foucart 2020). As a follow-up study, we hope to explore the scientific merit of conducting EM-GW follow-ups with the Vera C. Rubin Observatory, assuming the cadence and filter strategy for KN identification outlined in (Andreoni et al., 2021b), using the `nimbus` framework.

Constraining the ejecta masses of the KN population could potentially provide us better insights into the amount of r-process material contributed to the formation of KNe (Hotokezaka et al., 2018). It will also help in understanding the relationship and breaking the degeneracy that exists between binary parameters (equation of state, spin and mass ratio) (Foucart et al., 2018; Hinderer et al., 2019; Radice & Dai, 2019; Zhu et al., 2020), ejecta mass and KN light curve morphology. (Coughlin et al., 2019b; Hotokezaka & Nakar, 2020; Breschi et al., 2021; Raaijmakers et al., 2021). The future GW and EM multi-messenger landscape will provide the opportunity to explore this further.

CHAPTER 4

Conclusions and Future Directions

Gravitational-wave (GW) astronomy has provided us with new avenues for observing and studying the transient astrophysical universe. These include establishing a population of black holes and neutron stars in binaries which were previously undetected in the electromagnetic (EM) spectrum (Abbott et al., 2019a, 2021b; The LIGO Scientific Collaboration et al., 2021a), providing laboratories that test the nature of gravity in the strongest regimes (Abbott et al., 2019c, 2021c; The LIGO Scientific Collaboration et al., 2021c), shedding light on stellar and binary evolution models (de Mink & Mandel, 2016; Belczynski et al., 2020) and measuring the cosmic expansion history of the universe by estimating the Hubble constant (and B. P. Abbott et al., 2017; Abbott et al., 2021d). In addition, GW astronomy has opened a new era of multi-messenger astronomy with the direct detection of mergers involving neutron stars in both GW and EM spectra. Particularly, the detection of the "kilonova" from GW170817 Abbott et al. (2017c) by several EM telescopes around the globe, has already resulted in implications for nuclear theory viz. r-process nucleosynthesis and nuclear equation of state. Every new observing survey carried out by current as well as future GW detectors will enrich and update our understanding of the avenues mentioned above and, thereby, the universe. This dissertation has focused on two such areas of exploration — inferring the mass distribution of compact binaries using data solely from GW observations and inferring kilonova population properties using data from GW and EM observations. Both these studies have employed data-driven modeling techniques such as Gaussian processes and hierarchical Bayesian inference.

4.1 THE BINNED GAUSSIAN PROCESS MODEL

4.1.1 Summary

Chapter 2 describes modeling the mass distribution of compact binaries observed by the Advanced LIGO and Virgo detectors using the BINNED GAUSSIAN PROCESS (BGP) model presented in Section 2.3.1 and presents results using the latest catalog of GW observations (The LIGO Scientific Collaboration et al., 2021a). In contrast to studies that employ parametric models with a dependence on physical mass parameters to analyze the shape of the mass distribution, the BGP method uses a Gaussian process to model the rate densities in the 2-D parameter space of the component masses of the binary. Gaussian processes provide a flexible, mass-independent way to analyze these compact binaries. The BGP model also provides the ability to model the mass distribution across sub-populations including BNS, NSBH and BBH. The results shown in Section 2.4 highlight the importance of using flexible methods to model compact object populations in order to extract the presence of sub-structure which cannot be modeled using simple analytical functions. In particular, the local excess of black holes at $\sim 35M_{\odot}$ (seen in Figure 2.6) and capturing the transition of the mass distribution from NS to BH regimes (seen in Figure 2.5) are features that have the potential to inform binary formation channels and stellar evolution models (see references in Section 2.5). Results from the BGP model also show statistical agreement with other population models used to model the mass distribution for the latest GW catalog Abbott et al. (2021a). This includes the shape of mass distribution as well as the merger rate densities shown in Tables 2.2 and 2.3. Such statistical consistencies across models are essential to establish model robustness and will be an important feature of analysing GW catalogs in the future.

4.1.2 Limitations and Future Improvements

Section 2.5 also outlined the limitations of the BGP model used to obtain results in Chapter 2, that can be improved for future analyses. This included having the ability to model joint mass, redshift and spin distributions to test for the presence of correlations within the population defined by these physical source parameters. Specifically, with recent studies inferring correlations between the mass and spin parameters of binary black holes (Abbott et al., 2021a; Callister et al., 2021), such a functionality becomes even more relevant. Further the redshift dependence of the merger rate density in this study was fixed to one that is uniform as a function of the co-moving volume. However, as stated previously, current analyses are already finding the merger rate density to be increasing as function of redshift (Abbott et al., 2021e,a). Another scope for improvement is the relative increase in the resolution of the 2-D bins defining the BINNED GAUSSIAN PROCESS. In our specific study here, we have considered a 17-by-17 grid in the space of component masses as defined in Section 2.3.1. Such a grid enabled the inference of substructure within the population (especially for BBHs). Future population studies analysing GW catalogs would benefit from having more bins to resolve structure within the BNS and NSBH sub-populations as well. Although, the computational demands to accommodate denser grids might need to be investigated since the covariance calculations will scale in a quadratic fashion with the number of bins. The current BGP model presented here, is implemented using a single machine with multiple ($\sim 2-3$) Central Processing Unit (CPU) cores. In order to facilitate likelihood computations with denser grids, where parallelization might be critical, future analyses would need to implement the framework using Graphical Processing Units (GPUs).

4.2 THE NIMBUS FRAMEWORK

4.2.1 Summary

Chapter 3 focuses on a subset of GW merger events containing neutron stars. It describes a hierarchical Bayesian framework - `nimbus` - to infer the properties of the kilonova (Li & Paczyński, 1998; Rosswog, 2005; Metzger et al., 2010; Tanaka & Hotokezaka, 2013) emission from such mergers using the observed data from non-detections in electromagnetic surveys. Studying such merger events and the associated kilonova are especially of interest to the astronomy community since they are potential sites for the radioactive decay of r-process elements synthesized when neutron-rich ejecta from the merger powers the kilonova. Thus, kilonovae have the ability to inform fundamental nuclear physics such as r-process nucleosynthesis and nuclear equation of state. In addition, constraining kilonova population properties will provide insights into the multi-scale, multi-messenger physics of how neutron stars merge.

In chapter 3 we used the binary neutron star merger event GW190425, observed in Advanced LIGO-Virgo's third observing run O3, and follow-up observations from the Zwicky Transient Facility (ZTF) to test the `nimbus` framework using a single event. Assuming a linear evolution model for the associated kilonova, constraints on the initial absolute magnitude and decay rate were derived for two different prior choices for this parameter space. For uniform priors described in Section 3.3.1, the posterior probability distribution (see Figure 3.1) disfavors models of kilonovae that are initially brighter than ~ -18 mag and rise in their subsequent evolution. These results also show consistency with previous studies (Kasliwal et al., 2020). For the priors that are motivated from Monte-Carlo radiative transfer simulations of kilonovae (Coughlin et al., 2018b; Bulla, 2019), the posterior probability distribution (see Figure 3.5) is not informative with re-

spect to the corresponding prior distribution. These results demonstrate the potential of the framework to constrain kilonova population properties. We also compared the inferences derived from the framework with those from a simulator software - `simsurvey` (Feindt et al., 2019). As shown in Figure 3.4 besides qualitative differences that exist owing to differences in ideology and implementation, the comparisons are consistent with each other. Nonetheless, despite having the ability to incorporate the probability of astrophysical origin, finite sky-coverage and data from multiple electromagnetic passbands there are limitations that can be improved for future studies.

4.2.2 Limitations and Future Outlook

In the study presented in Chapter 3, we only made use of follow-up data from a single binary neutron star event — GW190425 — to demonstrate the functionality of the `nimbus` framework. On the other hand, Advanced LIGO-Virgo's third observing run had several other events for which follow-up observations were carried out by the Zwicky Transient Facility (ZTF) (Kasliwal et al., 2020). Future efforts should focus on extending the analysis presented here to include multiple events thereby obtaining kilonova population constraints using a population of events. Further, the kilonova evolution model assumed in the study is a single "average-band" linear model with respect to time and restricted to 3 days from the time of the merger event. Even though these model assumptions might enable a simpler analysis, it would be more suitable to consider realistic evolution models derived from simulations of kilonovae that account for color evolution and are more complex than simple linear functions. Finally, the entire formalism presented in Chapter 3 is based on using data from non-detections of kilonovae. Stronger constraints on the kilonova population might be derived if data from detected kilonova observations are included in the inference framework. As stated previously, this might necessitate

non-trivial changes to the formalism and require model selection effects conditioned on detection to be appropriately modeled.

4.3 USING COMPACT BINARY POPULATIONS TO INFORM KILONOVAE MODELS

We are entering an era where gravitational-wave source detections are becoming commonplace. Current gravitational-wave detectors at their design sensitivities (Buikema et al., 2020) and the future network of detectors (Punturo et al., 2010; Reitze et al., 2019; Sathyaprakash et al., 2019; Kalogera et al., 2019) hold the promise of delivering catalogs of compact binary observations which are orders of magnitude larger (Sathyaprakash et al., 2019) than our current set of detections. Such datasets will lead to stronger constraints on the mass distribution of compact binaries as outlined by previous studies including the results presented in Chapter 2. In particular, informative distributions for the component masses in systems with neutron stars can lead to data-driven simulations of the mergers of such systems. Such simulations will help inform the prior distribution of model parameters that define the evolution of kilonovae. Using inference frameworks as presented in Chapter 3 then will help place constraints on kilonovae population properties that are motivated by the observed sources.

BIBLIOGRAPHY

Aasi J., et al., 2015, Classical and Quantum Gravity, 32, 074001

Abadie J., et al., 2010a, Physical Review D, 82

Abadie J., et al., 2010b, The Astrophysical Journal, 715, 1453

Abbott B. P., et al., 2016a, Phys. Rev. X, 6, 041015

Abbott B., et al., 2016b, Physical Review X, 6

Abbott B. P., et al., 2016c, Phys. Rev. Lett., 116, 061102

Abbott B. P., et al., 2017a, Classical and Quantum Gravity, 34, 044001

Abbott B. P., et al., 2017b, Phys. Rev. Lett., 119, 161101

Abbott B. P., et al., 2017c, The Astrophysical Journal Letters, 848, L12

Abbott B. P., et al., 2017d, The Astrophysical Journal, 850, L39

Abbott B., et al., 2019a, Physical Review X, 9

Abbott B. P., et al., 2019b, Physical Review X, 9, 031040

Abbott B., et al., 2019c, Physical Review D, 100

Abbott B. P., et al., 2019d, The Astrophysical Journal, 882, L24

Abbott B. P., et al., 2020a

Abbott R., et al., 2020b, arXiv e-prints, p. arXiv:2010.14527

Abbott B. P., et al., 2020c, Living Reviews in Relativity, 23

Abbott R., et al., 2020d, Physical Review D, 102

Abbott R., et al., 2021a, The population of merging compact binaries inferred using gravitational waves through GWTC-3, doi:10.48550/ARXIV.2111.03634, https://arxiv.org/abs/2111.03634

Abbott R., et al., 2021b, Physical Review X, 11

Abbott R., et al., 2021c, Physical Review D, 103

Abbott B. P., et al., 2021d, The Astrophysical Journal, 909, 218

Abbott R., et al., 2021e, The Astrophysical Journal Letters, 913, L7

Abbott R., et al., 2021f, The Astrophysical Journal Letters, 915, L5

Abramovici A., et al., 1992, Science, 256, 325

Acernese F., et al., 2006, Classical and Quantum Gravity, 23, S635

Acernese F., et al., 2015, Class. Quant. Grav., 32, 024001

Anand S., et al., 2020, Nature Astronomy

Andreoni I., et al., 2017, Publications of the Astronomical Society of Australia, 34, e069

Andreoni I., Goldstein D., et al., 2020, Astrophys. J., 890, 131

Andreoni I., et al., 2021a, Fast-transient Searches in Real Time with ZTFReST: Identification of Three Optically-discovered Gamma-ray Burst Afterglows and New Constraints on the Kilonova Rate (arXiv:2104.06352)

Andreoni I., et al., 2021b, arXiv e-prints, p. arXiv:2111.01945

Antier, S. and Agayeva, S. and AlMualla, M. and others 2020

Antonini F., Rasio F. A., 2016, The Astrophysical Journal, 831, 187

Arcavi I., 2018, The Astrophysical Journal, 855, L23

Askar A., Sedda M. A., Giersz M., 2018, Monthly Notices of the Royal Astronomical Society, 478, 1844

Banerjee S., 2022, Physical Review D, 105

Barbieri C., Salafia O. S., Colpi M., Ghirlanda G., Perego A., 2021, Astronomy and Astrophysics, 654, A12

Barnes J., Kasen D., Wu M.-R., Martínez-Pinedo G., 2016, The Astrophysical Journal, 829, 110

Barnes J., Zhu Y. L., Lund K. A., Sprouse T. M., Vassh N., McLaughlin G. C., Mumpower M. R., Surman R., 2020, arXiv e-prints, p. arXiv:2010.11182

Barrett J. W., Gaebel S. M., Neijssel C. J., Vigna-Gó mez A., Stevenson S., Berry C. P. L., Farr W. M., Mandel I., 2018, Monthly Notices of the Royal Astronomical Society, 477, 4685

Bauswein A., Baumgarte T. W., Janka H.-T., 2013, Phys. Rev. Lett., 111, 131101

Belczynski K., Holz D. E., Bulik T., O'Shaughnessy R., 2016a, Nature, 534, 512

Belczynski K., et al., 2016b, Astronomy & Astrophysics, 594, A97

Belczynski K., et al., 2020, Astronomy & Astrophysics, 636, A104

Bellm E. C., et al., 2019, Publications of the Astronomical Society of the Pacific, 131, 018002

Blazek M., et al., 2019, GRB Coordinates Network, 24227, 1

Breschi M., Perego A., Bernuzzi S., Del Pozzo W., Nedora V., Radice D., Vescovi D., 2021, arXiv e-prints, p. arXiv:2101.01201

Buikema A., et al., 2020, Phys. Rev. D, 102, 062003

Bulla M., 2019, Monthly Notices of the Royal Astronomical Society, 489, 5037–5045

Callister T. A., Haster C.-J., Ng K. K. Y., Vitale S., Farr W. M., 2021, The Astrophysical Journal Letters, 922, L5

Chambers K. C., et al., 2016, arXiv e-prints, p. arXiv:1612.05560

Chornock R., et al., 2017, The Astrophysical Journal, 848, L19

Côté B., et al., 2018, The Astrophysical Journal, 855, 99

Coughlin M. W., et al., 2018a, Monthly Notices of the Royal Astronomical Society, 478, 692–702

Coughlin M. W., et al., 2018b, Monthly Notices of the Royal Astronomical Society, 480, 3871–3878

Coughlin M. W., et al., 2019a, Publications of the Astronomical Society of the Pacific, 131, 048001

Coughlin M. W., Dietrich T., Margalit B., Metzger B. D., 2019b, Monthly Notices of the Royal Astronomical Society: Letters, 489, L91

Coughlin M. W., et al., 2019c, Mon. Not. Roy. Astron. Soc., 492, 863

Coughlin M. W., et al., 2019d, The Astrophysical Journal, 885, L19

Coulter D. A., et al., 2017, Science, 358, 1556

Cowperthwaite P. S., et al., 2017, The Astrophysical Journal Letters, 848, L17

Creighton J., Anderson W., 2011, Gravitational-Wave Physics and Astronomy: An Introduction to Theory, Experiment and Data Analysis.

Cutler C., Thorne K. S., 2002, An Overview of Gravitational-Wave Sources, doi:10.48550/ARXIV.GR-QC/0204090, https://arxiv.org/abs/gr-qc/0204090

De K., et al., 2019, GRB Coordinates Network, 24187, 1

Dekany R., et al., 2020, Publications of the Astronomical Society of the Pacific, 132, 038001

Dhawan S., Bulla M., Goobar A., Sagués Carracedo A., Setzer C. N., 2020, The Astrophysical Journal, 888, 67

Dietrich T., Coughlin M. W., Pang P. T. H., Bulla M., Heinzel J., Issa L., Tews I., Antier S., 2020, Science, 370, 1450

Doctor Z., Wysocki D., O'Shaughnessy R., Holz D. E., Farr B., 2020, The Astrophysical Journal, 893, 35

Drout M. R., et al., 2017, Science, 358, 1570

Dudi R., et al., 2021, arXiv e-prints, p. arXiv:2109.04063

Einstein A., 1916, Annalen der Physik, 354, 769

Etienne Z. B., Liu Y. T., Shapiro S. L., Baumgarte T. W., 2009, Phys. Rev. D, 79, 044024

Evans P. A., et al., 2017, Science, 358, 1565

Farr W. M., Gair J. R., Mandel I., Cutler C., 2015a, Phys. Rev. D, 91, 023005

Farr W. M., Gair J. R., Mandel I., Cutler C., 2015b, Phys. Rev. D, 91, 023005

Feindt U., Nordin J., Rigault M., Brinnel V., Dhawan S., Goobar A., Kowalski M., 2019, Journal of Cosmology and Astroparticle Physics, 2019, 005–005

Fishbach M., Holz D. E., 2017, The Astrophysical Journal, 851, L25

Fishbach M., Holz D. E., Farr B., 2017, The Astrophysical Journal, 840, L24

Fishbach M., Holz D. E., Farr W. M., 2018, The Astrophysical Journal Letters, 863, L41

Foley R. J., Coulter D. A., Kilpatrick C. D., Piro A. L., Ramirez-Ruiz E., Schwab J., 2020, Monthly Notices of the Royal Astronomical Society, 494, 190

Ford K. E. S., McKernan B., 2021,] 10.48550/ARXIV.2109.03212

Foreman-Mackey D., Hogg D. W., Morton T. D., 2014, The Astrophysical Journal, 795, 64

Foucart F., Hinderer T., Nissanke S., 2018, Phys. Rev. D, 98, 081501

Foucart F., Moesta P., Ramirez T., Wright A. J., Darbha S., Kasen D., 2021, arXiv e-prints, p. arXiv:2109.00565

Fragione G., Grishin E., Leigh N. W. C., Perets H. B., Perna R., 2019, Monthly Notices of the Royal Astronomical Society, 488, 47

Freire P. C. C., Ransom S. M., Bégin S., Stairs I. H., Hessels J. W. T., Frey L. H., Camilo F., 2008, The Astrophysical Journal, 675, 670

Gaebel S. M., Veitch J., Dent T., Farr W. M., 2019, Monthly Notices of the Royal Astronomical Society, 484, 4008

Ghosh S., Chatterjee D., Kaplan D. L., Brady P. R., Sistine A. V., 2017, Publications of the Astronomical Society of the Pacific, 129, 114503

Giacobbo N., Mapelli M., 2018, Monthly Notices of the Royal Astronomical Society, 480, 2011

Gompertz B., et al., 2020

Górski K. M., Hivon E., Banday A. J., Wandelt B. D., Hansen F. K., Reinecke M., Bartelmann M., 2005, The Astrophysical Journal, 622, 759

Graham M. J., et al., 2019, Publications of the Astronomical Society of the Pacific, 131, 078001

Green G., 2018, The Journal of Open Source Software, 3, 695

Heger A., Woosley S. E., 2002, The Astrophysical Journal, 567, 532

Heger A., Fryer C. L., Woosley S. E., Langer N., Hartmann D. H., 2003, The Astrophysical Journal, 591, 288

Heinzel J., et al., 2021, Monthly Notices of the Royal Astronomical Society,

Hinderer T., et al., 2019, Phys. Rev. D, 100, 063021

Hoang B.-M., Naoz S., Kocsis B., Rasio F. A., Dosopoulou F., 2018, The Astrophysical Journal, 856, 140

Hong J., Vesperini E., Askar A., Giersz M., Szkudlarek M., Bulik T., 2018, Monthly Notices of the Royal Astronomical Society, 480, 5645

Hosseinzadeh G., et al., 2019, The Astrophysical Journal Letters, 880, L4

Hotokezaka K., Nakar E., 2020, The Astrophysical Journal, 891, 152

Hotokezaka K., Kiuchi K., Kyutoku K., Okawa H., Sekiguchi Y.-i., Shibata M., Taniguchi K., 2013, Phys. Rev. D, 87, 024001

Hotokezaka K., Beniamini P., Piran T., 2018, International Journal of Modern Physics D, 27, 1842005

Hotokezaka K., Nakar E., Gottlieb O., Nissanke S., Masuda K., Hallinan G., Mooley K. P., Deller A. T., 2019, Nature Astronomy, 3, 940

Hulse R. A., Taylor J. H., 1975, The Astrophysical Journal Letters, 195, L51

Inayoshi K., Haiman Z., Ostriker J. P., 2016, Monthly Notices of the Royal Astronomical Society, 459, 3738

Just O., Kullmann I., Goriely S., Bauswein A., Janka H.-T., Collins C. E., 2021, arXiv e-prints, p. arXiv:2109.14617

Kalogera V., et al., 2019, Deeper, Wider, Sharper: Next-Generation Ground-Based Gravitational-Wave Observations of Binary Black Holes, doi:10.48550/ARXIV.1903.09220, https://arxiv.org/abs/1903.09220

Kasen D., Fernández R., Metzger B. D., 2015, Monthly Notices of the Royal Astronomical Society, 450, 1777

Kasen D., Metzger B., Barnes J., Quataert E., Ramirez-Ruiz E., 2017, Nature, 551, 80

Kasliwal M. M., 2011, PhD thesis, California Institute of Technology

Kasliwal M. M., et al., 2017, Science, 358, 1559

Kasliwal M. M., et al., 2019a, Monthly Notices of the Royal Astronomical Society,

Kasliwal M. M., et al., 2019b, GRB Coordinates Network, 24191, 1

Kasliwal M. M., et al., 2020, Kilonova Luminosity Function Constraints based on Zwicky Transient Facility Searches for 13 Neutron Star Mergers (arXiv:2006.11306)

Kawaguchi K., Kyutoku K., Shibata M., Tanaka M., 2016, The Astrophysical Journal, 825, 52

Kawaguchi K., Shibata M., Tanaka M., 2020, The Astrophysical Journal, 889, 171

Kilpatrick C. D., et al., 2017, Science, 358, 1583

Kiuchi K., Kyutoku K., Shibata M., Taniguchi K., 2019, The Astrophysical Journal, 876, L31

Korobkin O., et al., 2020, arXiv e-prints, p. arXiv:2004.00102

Kovetz E. D., Cholis I., Breysse P. C., Kamionkowski M., 2017, Phys. Rev. D, 95, 103010

Krüger C. J., Foucart F., 2020, Physical Review D, 101, 103002

Kulkarni S. R., Hut P., McMillan S., 1993, Nature, 364, 421

Kullmann I., Goriely S., Just O., Ardevol-Pulpillo R., Bauswein A., Janka H.-T., 2021, Monthly Notices of the Royal Astronomical Society

Kyutoku K., Ioka K., Okawa H., Shibata M., Taniguchi K., 2015, Phys. Rev. D, 92, 044028

Kyutoku K., Fujibayashi S., Hayashi K., Kawaguchi K., Kiuchi K., Shibata M., Tanaka M., 2020, The Astrophysical Journal Letters, 890, L4

Köppel S., Bovard L., Rezzolla L., 2019, The Astrophysical Journal, 872, L16

LIGO Scientific Collaboration Virgo Collaboration KAGRA Collaboration 2021, The population of merging compact binaries inferred using gravitational waves through GWTC-3 - Data release, doi:10.5281/zenodo.5655785, https://doi.org/10.5281/zenodo.5655785

Levan A., 2020, PoS, Asterics2019, 044

Li L.-X., Paczyński B., 1998, The Astrophysical Journal, 507, L59–L62

Li B., Xu D., Zhou X., Lu H., 2019, GRB Coordinates Network, 24285, 1

Lipunov V. M., et al., 2017, The Astrophysical Journal Letters, 850, L1

Lipunov V., et al., 2019, GRB Coordinates Network, 24167, 1

Loredo T. J., 2004, in Fischer R., Preuss R., Toussaint U. V., eds, American Institute of Physics Conference Series Vol. 735, Bayesian Inference and Maximum Entropy Methods in Science and Engineering: 24th International Workshop on Bayesian Inference and Maximum Entropy Methods in Science and Engineering. pp 195–206 (arXiv:astro-ph/0409387), doi:10.1063/1.1835214

Lück H., et al., 2006, Classical and Quantum Gravity, 23, S71

Lundquist M. J., et al., 2019a, The Astrophysical Journal Letters, 881, L26

Lundquist M. J., et al., 2019b, GRB Coordinates Network, 24172, 1

Malmquist K. G., 1922, Meddelanden fran Lunds Astronomiska Observatorium Serie I, 100, 1

Malmquist K. G., 1925, Meddelanden fran Lunds Astronomiska Observatorium Serie I, 106, 1

Mandel I., Farr W. M., Colonna A., Stevenson S., Tiň o P., Veitch J., 2016, Monthly Notices of the Royal Astronomical Society, 465, 3254

Mandel I., Farr W. M., Gair J. R., 2019a, Monthly Notices of the Royal Astronomical Society, 486, 1086

Mandel I., Farr W. M., Gair J. R., 2019b, Monthly Notices of the Royal Astronomical Society, 486, 1086

Marchant P., Renzo M., Farmer R., Pappas K. M. W., Taam R. E., de Mink S. E., Kalogera V., 2019, The Astrophysical Journal, 882, 36

Margalit B., Metzger B. D., 2017, The Astrophysical Journal, 850, L19

Masci F. J., et al., 2019, Publications of the Astronomical Society of the Pacific, 131, 018003

McBrien O., et al., 2019, GRB Coordinates Network, 24197, 1

McCully C., et al., 2017, The Astrophysical Journal Letters, 848, L32

McKernan B., Ford K. E. S., O'Shaugnessy R., Wysocki D., 2020, Monthly Notices of the Royal Astronomical Society, 494, 1203

Metzger B. D., 2019, Living Reviews in Relativity, 23

Metzger B. D., et al., 2010, Monthly Notices of the Royal Astronomical Society, 406, 2650

Miller M., Yunes N., 2019, Nature, 568, 469

Mohite S. R., 2021, nimbus : A Bayesian inference framework to constrain kilonova models., doi:10.5281/zenodo.5648468, https://doi.org/10.5281/zenodo.5648468

Mohite S. R., et al., 2022, The Astrophysical Journal, 925, 58

Morgan R., et al., 2020, The Astrophysical Journal, 901, 83

Nakar E., 2019

Nicholl M., et al., 2017, The Astrophysical Journal Letters, 848, L18

Nicholl M., Margalit B., Schmidt P., Smith G. P., Ridley E. J., Nuttall J., 2021, arXiv e-prints, p. arXiv:2102.02229

Pedregosa F., et al., 2011, Journal of Machine Learning Research, 12, 2825

Perego A., Radice D., Bernuzzi S., 2017, The Astrophysical Journal Letters, 850, L37

Petrov P., et al., 2021, arXiv e-prints, p. arXiv:2108.07277

Pian E., et al., 2017, Nature, 551, 67

Punturo M., et al., 2010, Class. Quant. Grav., 27, 194002

Raaijmakers G., et al., 2021

Radice D., Dai L., 2019, European Physical Journal A, 55, 50

Radice D., Perego A., Hotokezaka K., Fromm S. A., Bernuzzi S., Roberts L. F., 2018, The Astrophysical Journal, 869, 130

Rasmussen C. E., Williams C. K. I., 2005, Gaussian Processes for Machine Learning. The MIT Press, doi:10.7551/mitpress/3206.001.0001, https://doi.org/10.7551/mitpress/3206.001.0001

Reitze D., et al., 2019,] 10.48550/ARXIV.1903.04615

Roberts L. F., Kasen D., Lee W. H., Ramirez-Ruiz E., 2011, The Astrophysical Journal Letters, 736, L21

Rodriguez C. L., Morscher M., Pattabiraman B., Chatterjee S., Haster C.-J., Rasio F. A., 2015, Physical Review Letters, 115

Rodriguez C. L., Chatterjee S., Rasio F. A., 2016, Physical Review D, 93

Romero-Shaw I. M., Kremer K., Lasky P. D., Thrane E., Samsing J., 2021, Monthly Notices of the Royal Astronomical Society, 506, 2362

Rosswog S., 2005, The Astrophysical Journal, 634, 1202

Rosswog S., Feindt U., Korobkin O., Wu M. R., Sollerman J., Goobar A., Martinez-Pinedo G., 2017, Classical and Quantum Gravity, 34, 104001

Safarzadeh M., Haiman Z., 2020, The Astrophysical Journal Letters, 903, L21

Sagués Carracedo A., Bulla M., Feindt U., Goobar A., 2021, Monthly Notices of the Royal Astronomical Society, 504, 1294

Salvatier J., Wiecki T. V., Fonnesbeck C., 2016, PeerJ Computer Science, 2, e55

Sasada M., et al., 2021, Progress of Theoretical and Experimental Physics, 2021, 05A104

Sathyaprakash B. S., et al., 2019, Cosmology and the Early Universe, doi:10.48550/ARXIV.1903.09260, https://arxiv.org/abs/1903.09260

Schlafly E. F., Finkbeiner D. P., 2011, The Astrophysical Journal, 737, 103

Shappee B. J., et al., 2017, Science, 358, 1574

Siegel D. M., 2019, European Physical Journal A, 55, 203

Singer L. P., Price L. R., 2016, Phys. Rev. D, 93, 024013

Singer L. P., et al., 2016a, The Astrophysical Journal Supplement Series, 226, 10

Singer L. P., et al., 2016b, The Astrophysical Journal, 829, L15

Smartt S. J., et al., 2017, Nature, 551, 75

Smith K., Young D., McBrien O., et al., 2019, GRB Coordinates Network, 24210, 1

Soares-Santos M., Holz D., Annis J., Chornock R., Herner K., 2017, Astrophys. J. Lett., 848, L16

Steeghs D., et al., 2019, GRB Coordinates Network, 24224, 1

Stevenson S., Ohme F., Fairhurst S., 2015, The Astrophysical Journal, 810, 58

Stevenson S., Sampson M., Powell J., Vigna-Gómez A., Neijssel C. J., Szécsi D., Mandel I., 2019, The Astrophysical Journal, 882, 121

Takahashi R., TAMA Collaboration 2004, Classical and Quantum Gravity, 21, S403

Talbot C., Thrane E., 2018, The Astrophysical Journal, 856, 173

Tanaka M., 2016, Advances in Astronomy, 2016, 634197

Tanaka M., Hotokezaka K., 2013, The Astrophysical Journal, 775, 113

Tanaka M., et al., 2017, Publications of the Astronomical Society of Japan, 69, 102

Tanaka M., et al., 2018, The Astrophysical Journal, 852, 109

Tanvir N. R., et al., 2017, The Astrophysical Journal Letters, 848, L27

The LIGO Scientific Collaboration The Virgo Collaboration 2009, Nature, 460, 990

The LIGO Scientific Collaboration et al., 2010, Sensitivity to Gravitational Waves from Compact Binary Coalescences Achieved during LIGO's Fifth and Virgo's First Science Run, doi:10.48550/ARXIV.1003.2481, https://arxiv.org/abs/1003.2481

The LIGO Scientific Collaboration et al., 2021a, GWTC-3: Compact Binary Coalescences Observed by LIGO and Virgo During the Second Part of the Third Observing Run, doi:10.48550/ARXIV.2111.03606, https://arxiv.org/abs/2111.03606

The LIGO Scientific Collaboration Virgo Collaboration KAGRA Collaboration 2021b, GWTC-3: Compact Binary Coalescences Observed by LIGO and Virgo During the Second Part of the Third Observing Run — O3 search sensitivity estimates, doi:10.5281/zenodo.5546676, https://doi.org/10.5281/zenodo.5546676

The LIGO Scientific Collaboration et al., 2021c, Tests of General Relativity with GWTC-3, doi:10.48550/ARXIV.2112.06861, https://arxiv.org/abs/2112.06861

Thrane E., Talbot C., 2019, Publications of the Astronomical Society of Australia, 36

Tiwari V., 2018, Classical and Quantum Gravity, 35, 145009

Tiwari V., 2021, Classical and Quantum Gravity, 38, 155007

Tonry J. L., et al., 2018, Publications of the Astronomical Society of the Pacific, 130, 064505

Utsumi Y., et al., 2017, Publications of the Astronomical Society of Japan, 69, 101

Veitch J., et al., 2015a, Phys. Rev. D, 91, 042003

Veitch J., et al., 2015b, Physical Review D, 91, 042003

Vitale S., Gerosa D., Farr W. M., Taylor S. R., 2021, in , Handbook of Gravitational Wave Astronomy. Springer Singapore, pp 1–60, doi:10.1007/978-981-15-4702-7_45-1, https://doi.org/10.1007%2F978-981-15-4702-7_45-1

Waxman E., Ofek E. O., Kushnir D., Gal-Yam A., 2018, Monthly Notices of the Royal Astronomical Society, 481, 3423

Weisberg J. M., Taylor J. H., 2005, in Rasio F. A., Stairs I. H., eds, Astronomical Society of the Pacific Conference Series Vol. 328, Binary Radio Pulsars. p. 25 (arXiv:astro-ph/0407149)

Wiktorowicz G., Wyrzykowski Ł., Chruslinska M., Klencki J., Rybicki K. A., Belczynski K., 2019, The Astrophysical Journal, 885, 1

Wollaeger R. T., et al., 2018, Monthly Notices of the Royal Astronomical Society, 478, 3298

Wong K. W., Breivik K., Kremer K., Callister T., 2021, Physical Review D, 103

Woosley S. E., 2017, The Astrophysical Journal, 836, 244

Woosley S. E., Heger A., 2021, The Astrophysical Journal Letters, 912, L31

Wu M.-R., Barnes J., Martínez-Pinedo G., Metzger B. D., 2019, Phys. Rev. Lett., 122, 062701

Wysocki D., Gerosa D., O'Shaughnessy R., Belczynski K., Gladysz W., Berti E., Kesden M., Holz D. E., 2018, Physical Review D, 97

Wysocki D., Lange J., O'Shaughnessy R., 2019, Physical Review D, 100

Xu D., et al., 2019, GRB Coordinates Network, 24190, 1

Yang Y., et al., 2019, Physical Review Letters, 123

Zevin M., et al., 2021, The Astrophysical Journal, 910, 152

Zhu Y., et al., 2018, The Astrophysical Journal, 863, L23

Zhu J.-P., et al., 2020, arXiv e-prints, p. arXiv:2011.02717

Zhu J.-P., Yang Y.-P., Zhang B., Gao H., Yu Y.-W., 2021, arXiv e-prints, p. arXiv:2110.10468

and B. P. Abbott et al., 2017, Nature, 551, 85

de Jaeger T., et al., 2021, Monthly Notices of the Royal Astronomical Society, 509, 3427–3440

de Mink S. E., Mandel I., 2016, Monthly Notices of the Royal Astronomical Society, 460, 3545

van Son L. A. C., et al., 2020, The Astrophysical Journal, 897, 100

Özel F., Freire P., 2016, Annual Review of Astronomy and Astrophysics, 54, 401

Siddharth Rajiv Mohite

Personal Information

Affiliations	PhD Student, University of Wisconsin-Milwaukee (UWM) GROWTH Collaboration (Member) LSSTC Data Science Fellow LIGO Scientific Collaboration (Member) NANOGrav Collaboration (Associate Member) Visiting Researcher at Flatiron Institute, NY
Contact Details	srmohite@uwm.edu +1 414-554-9132

Education

2016 – 2022	**Doctor of Philosophy (PhD) in Physics** Department of Physics, University of Wisconsin-Milwaukee
2010 – 2015	**Bachelor and Master of Science** Indian Institute of Science Education and Research (IISER), Pune

Research Experience

2017 – 2021	Dissertator Fellow/Graduate Research Assistant, *Dept. Of Physics, UWM* **Project Title :** Population inference of compact binaries using Gaussian processes and observations of gravitational-wave events from LIGO-Virgo. **Advisor :** Prof. Jolien Creighton
2020 – 2022	Dissertator Fellow/Graduate Research Assistant, *Dept. Of Physics, UWM* **Project Title :** Understanding the kilonovae population using hierarchical bayesian inference and observations from the Zwicky Transient Facility (ZTF). **Advisor :** Prof. David Kaplan
2021 – *present*	Research Analyst, *Center for Computational Astrophysics, Flatiron Institute* **Project Title :** Mapping the effects of eccentricity and circumbinary-gas on the local population of supermassive binary black holes using observations from the 2 Micron All-Sky Survey (2MASS) Survey. **Advisor :** Prof. Chiara Mingarelli

Fellowships & Awards

2021 – 2022	UWM Distinguished Dissertator Fellowship *Fellowship includes $16500 stipend, full academic-year tuition, health benefits, and a $1000 travel award.*
2021	Center for Computational Astrophysics (CCA) Pre-Doc Fellowship *A 5-month research internship ($23000 stipend, tuition and health benefits)*

Fellowships & Awards *(continued)*

2018 – 2021	LSSTC Data Science Fellowship *A two-year training program (6 one-week schools), designed to teach astronomy students essential skills for dealing with big data from LSST.*
2016 – 2021	Physics Research Excellence and Chancellors Graduate Student Awards *Semester-based academic excellence awards ($22000 across 10 semesters).*
2017	David Lichtman Research Fellowship *Summer research fellowship ($3000).*
2010 – 2015	INSPIRE Fellow *Merit-based fellowship including tuition, living stipend, and a research grant.*
2014	Indian Academy of Science (IAS) Summer Fellow
2011	Academic Excellence Award

Skills

Programming:	Proficient in Python, UNIX Basic knowledge of C, MATLAB.
Data and Software:	Proficient in Pandas, Git, Software development Experience with SQL, CI, Unit Testing, Google Colab.
Machine Learning:	Skilled in implementing Gaussian Processes, K-nearest Neighbors, Random Forests, Support Vector Machines, Deep Neural Networks with scikit-learn and TensorFlow.
High-performance computing:	Proficient in high-throughput parallel computing using HTCondor and Slurm.

Publications

(Short Author Papers)

1. Mohite, Siddharth R., et al. "Inferring Kilonova Population Properties with a Hierarchical Bayesian Framework. I. Nondetection Methodology and Single-event Analyses." The Astrophysical Journal 925.1 (2022): 58.

2. Sachdev, Surabhi, et al. "An early-warning system for electromagnetic follow-up of gravitational-wave events." The Astrophysical Journal Letters 905.2 (2020): L25.

3. Kasliwal, Mansi M., et al. "Kilonova Luminosity Function Constraints Based on Zwicky Transient Facility Searches for 13 Neutron Star Merger Triggers during O3." The Astrophysical Journal 905.2 (2020): 145.

4. Kapadia, Shasvath J., et al. "A self-consistent method to estimate the rate of compact binary coalescences with a Poisson mixture model." Classical & Quantum Gravity 37.4 (2020): 045007.

Publications *(continued)*

5. Messick, Cody, et al. "Automating the Inclusion of Subthreshold Signal-to-Noise Ratios for Rapid Gravitational-Wave Localization." arXiv preprint arXiv:2011.02457 (2020).

6. Chan, Chiwai, et al. "Improving the background estimation technique in the GstLAL inspiral pipeline with the time-reversed template bank." arXiv preprint arXiv:2009.03025 (2020).

7. Magee, Ryan, et al. "Sub-threshold binary neutron star search in advanced ligo's first observing run." The Astrophysical Journal Letters 878.1 (2019): L17.

(Collaboration Papers with substantial contributions)

8. LIGO Scientific Collaboration, Virgo Collaboration, and KAGRA Scientific Collaboration. "The population of merging compact binaries inferred using gravitational waves through GWTC-3." arXiv preprint arXiv:2111.03634 (2021).

9. Andreoni, Igor, et al. "GROWTH on S190814bv: Deep Synoptic Limits on the Optical/Near-infrared Counterpart to a Neutron Star–Black Hole Merger." The Astrophysical Journal 890.2 (2020): 131.

10. Abbott, Rich, et al. "Open data from the first and second observing runs of Advanced LIGO and Advanced Virgo." SoftwareX 13 (2021): 100658.

Conferences/Schools Attended

2018 – 2021	LSSTC Data Science Fellowship Program
2018	Midwest Relativity Meeting, University of Wisconsin - Milwaukee
2018	Summer School on Neutron Star Mergers, Facility for Rare Isotope Beams (FRIB), Michigan State University, East Lansing
2017	Midwest Relativity Meeting, University of Michigan – Ann Arbor

Teaching & Science Outreach

2018 – *present*	Member of CoffeeShop Astrophysics (http://www.cgca.uwm.edu/coffee/index.html).
2016 – 2018	Graduate Student Instructor for PHY120 (Classical Mechanics) and PHY122 (Electromagnetism)
2010 – 2015	Member of Disha (initiative to teach under-privileged school children) (http://www.iiserpune.ac.in/outreach/social-outreach/disha)

References

Jolien Creighton (Ph.D. Supervisor)
University of Wisconsin-Milwaukee
jolien[at]uwm.edu

David Kaplan
University of Wisconsin-Milwaukee
kaplan[at]uwm.edu

Chiara Mingarelli
University of Connecticut
chiara.mingarelli[at]uconn.edu